In vitro maturation of NiSOD reveals a role for cytoplasmic histidine in processing and metalation

Priyanka Basak[1], Diane E. Cabelli[2], Peter T. Chivers[3*], Erik R. Farquhar[4], Michael J. Maroney[1,5*]

[1]Department of Chemistry, University of Massachusetts Amherst MA 01003, USA; [2]Department of Chemistry, Building 555A, Brookhaven National Laboratory, P.O. Box 5000, Upton, New York 11973, USA; [3]Departments of Biosciences and Chemistry, Durham University, Durham, DH1 3LE, United Kingdom; [4]National Synchrotron Light Source-II, Brookhaven National Laboratory, Upton, NY 11973; [5]Program in Molecular and Cellular Biology, University of Massachusetts, Amherst, MA 01003, USA

*Corresponding authors: mmaroney@chem.umass.edu; peter.chivers@durham.ac.uk

ABSTRACT

The importance of cellular low molecular weight (LMW) ligands in metalloenzyme maturation is largely unexplored. Maturation of NiSOD requires post-translational N-terminal processing of the proenzyme, SodN, by its cognate protease, SodX. Here we provide evidence for the participation of L-histidine in the protease-dependent maturation of Nickel-dependent Superoxide Dismutase (NiSOD) from *Streptomyces coelicolor*. *In vitro* studies using purified proteins cloned from *S. coelicolor* and overexpressed in *E. coli* support a model where a ternary complex formed between the substrate (SodN), the protease (SodX) and L-Histidine creates a novel Ni-binding site that is capable of the N-terminal processing of SodN and specifically incorporates Ni into the apo-NiSOD product. Thus, L-Histidine serves many of the functions associated with a metallochaperone or, conversely, eliminates the need for a metallochaperone in NiSOD maturation.

GRAPHICAL ABSTRACT

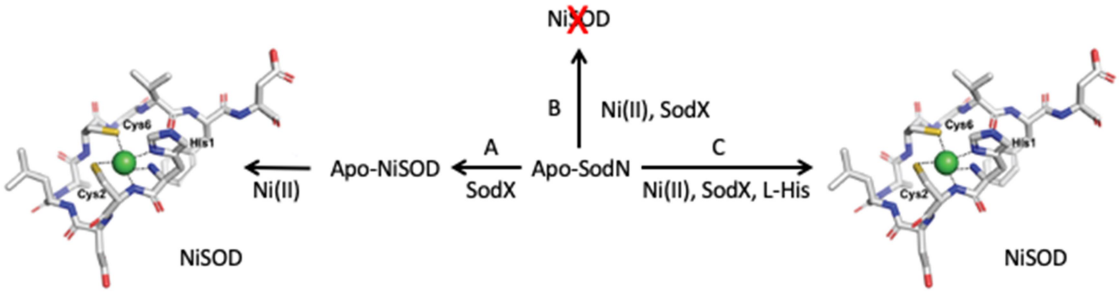

INTRODUCTION

An emerging theme in bacterial cellular metal trafficking is the importance of the cytosolic labile metal pool comprised of metals bound to low molecular weight species.[1, 2] Metals bind small molecules, including amino acids, metabolites (*e.g.,* citrate), and thiols, (*e.g.*, glutathione), with speciation influenced by concentration and metal preferences for ligand identity and coordination geometry. For example, upon lysis of anaerobically grown *E. coli,* Ni(II) is found distributed between complexes with histidine, aspartate, ATP, or oxidized glutathione.[3] While low molecular weight complexes can play a role in defense against metal stress, the roles of these species in metal trafficking and homeostasis is less well known.[4] In bacteria, metal regulators sense the abundance of these LMW species, referred to as the buffer, and alter gene expression to match metal supply with demand.[4-7] Precedence for protein recognition of specific complexes of L-His, and not D-His, has been demonstrated in bacterial trans-membrane import of Ni(II) via the bacterial NikA(BCDE) transporter system.[8, 9] Evidence for the participation of the labile metal pool in metalloenzyme maturation was heretofore unexamined.

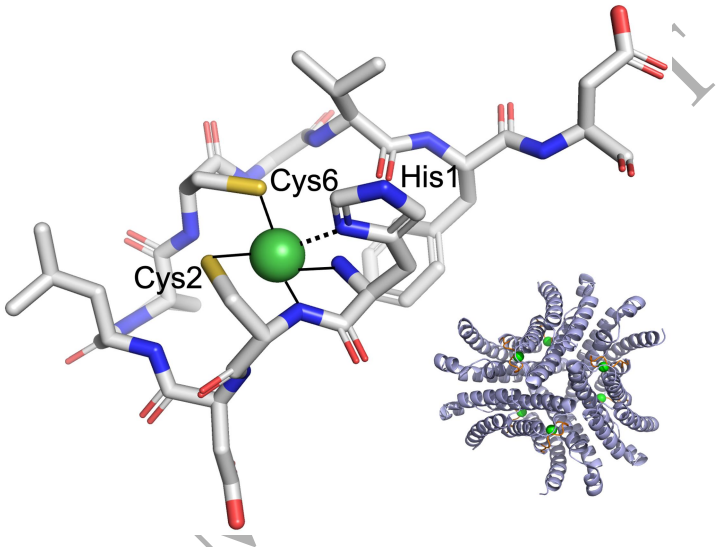

Fig. 1. The nickel active site in NiSOD (PDB ID: 1T6U). The inset shows the hexameric enzyme viewed down a 3-fold axis. Green spheres represent nickel atoms. The oxidized enzyme is 50:50 mixture of Ni(II) and Ni(III) where the latter is stabilized by an additional His1 coordination (dashed line).

Nickel Superoxide Dismutase (NiSOD) is the nickel-specific member of the SOD class of enzymes that catalyze the disproportionation of toxic superoxide radical to oxygen and hydrogen

peroxide.[10-13] NiSOD has been found in actinobacteria (*e.g., Streptomyces sp.*) and cyanobacteria (*e.g. Prochlorococcus sp.*) and is expressed in response to Ni(II) in *Streptomyces lividans.*[14, 15] Its presence in cyanobacteria makes it the most abundant SOD in the ocean.[16] The enzyme employs unique structural features at the N-terminus (*e.g.,* Cys ligation, **Fig. 1**).[12, 17-20] Although the structural, spectroscopic, and enzymatic properties of NiSOD are well-characterized, the maturation process that inserts nickel into this enzyme remains elusive.[19, 21]

NiSOD is the post-translationally modified product of *sodN*, which encodes an inactive pro-enzyme that has a variable N-terminal leader sequence (14 residues in *S. coelicolor* SodN) upstream of the His residue (**Fig. S1**) that is the N-terminus of the mature enzyme.[22, 23] The physiological function of the leader sequence is still unknown. Prior to the identification of SodX, the endopeptidase that removes the N-terminal extension *in vivo*, active NiSOD was obtained *in vitro* using engineered constructs of SodN with a cleavable tag (such as Factor-Xa or PelB cleavage sites) to effect N-terminal processing.[12, 23] After processing, the resulting recombinant apo-NiSOD was readily nickelated by Ni(II) *in vitro*, consistent with metallochaperone-independent maturation, and no candidate for a metallochaperone has yet been identified.[24] Proteolysis of the conserved Ala_{14}-His_{15} peptide bond (**Fig. S1**) in SodN is performed by SodX (encoded by *orf*X) and has been shown to be an absolute requirement for active NiSOD formation when heterologously co-expressed in *E. coli,* which naturally lacks both *sodN* and *orfX.*[13, 22, 25] These observations demonstrate that no species-specific metallochaperone is required for NiSOD assembly but do not illuminate how nickel is incorporated into the processed protein *in vivo*.

For NiSOD, the lack of a specific nickel metallochaperone in the *in vivo* study supports the notion that none is required for nickelation of apo-NiSOD under physiological conditions. In-

gel SOD activity assays performed on the *E. coli* cell lysates showed increasing NiSOD activity as a function of Ni(II) concentration.[25] Based on these *in vivo* results, as well as structural studies of Met0-NiSOD (insertion of a Met residue before His1 in the recombinant construct), CN^- treated apo-NiSOD, and analogy with the maturation of [NiFe]-hydrogenase, which requires nickel insertion prior to proteolysis of the large subunit, maturation of SodN was proposed to involve a nickel-dependent proteolysis by SodX. [12, 22, 25-27] It was postulated that chelation of Ni(II) by His15 and Cys16 in SodN (which becomes His1 and Cys2 in NiSOD) promotes proteolytic maturation followed by a *trans-cis* isomerization of Pro5 (Pro19 in SodN) that positions Cys6 so that the two thiols (Cys2 and Cys6) can bind nickel in a cis-orientation, thereby completing the nickel site coordination and forming the 'nickel-hook' feature of the mature enzyme.[12]

Here, we show that SodN can be processed *in vitro* by SodX in the absence of Ni(II) and subsequently nickelated to give active NiSOD, demonstrating the minimal molecular requirements for the maturation and activation of NiSOD. The inclusion of metal ions (including Ni(II)) in the proteolysis reaction mixture *inhibits* N-terminal processing by SodX. Critically, the inclusion of L-His (but not D-His) in the reaction mixture restores *in vitro* protein processing in the presence of Ni(II). The addition of His alone inhibits processing of SodN, indicating that under cellular conditions both histidine and Ni(II) are required for correct processing. The effect of L-His was shown to be Ni-specific, as Co(II) does not rescue SodN processing. XAS analysis of Ni-SodN complexes with or without His reveal that a putative ternary complex, NiSodN•His, has a four- or five-coordinate, low-spin Ni site with 1-2 S-donor ligands, and more closely resembles the Ni site in NiSOD. The Ni(II)•SodN complex has six-coordinate (N/O) high-spin complex with a His imidazole ligand but no S-donor ligands. These observations indicate that

SodN processing requires formation of a ternary complex of SodN, Ni(II), and histidine to ensure the fidelity of nickel insertion into apo-NiSOD.

RESULTS

Biochemical, biophysical and spectroscopic characterization of SodN

While the mature enzyme (apo-NiSOD) has been previously purified using various methods, the precursor, SodN has not been previously purified and characterized. Heterologously overexpressed and purified recombinant SodN **(Fig. S2, lane 4)** had the expected amino acid sequence **(Fig. S1)** and molecular weight **(Table 1; Fig. S3a, top)**, and was shown to be hexameric (SEC-MALS) and largely α-helical (CD), as is apo-NiSOD **(Fig. S3b,c).**[12, 28] In addition to the expected SodN monomers at 14,701 Da, the mass spectra show the presence of two N-terminally truncated species at 14,236 Da and 14,101 Da (denoted as NΔ4-SodN and NΔ5-SodN, that lack the first four and five residues, respectively **(Fig. S3a(top), d)**. These species occur in all batches of purification and are also detected in a variant of SodN used in this study (H15A-SodN; *vide infra*), and are likely to be an artifact of purification possibly arising via autocleavage when changing pH from 8.8 to 7.0, as has been observed for other proteins with unstable sequences.[29] A peak corresponding to a +32 modification of SodN was also observed in some samples and is tentatively assigned to the presence of sulfoxycysteine species (disulfenate or sulfinate), as previously observed for a variant of NiSOD.[30]

To understand the intrinsic Ni(II)-binding properties of SodN prior to processing and to compare them with those of the processed protein (NiSOD), Ni(II)-binding to apo-WT-SodN and H15A-SodN was examined using isothermal titration calorimetry (ITC) **(Fig. 2)**. The binding isotherm for SodN is consistent with a single Ni-binding event involving 1.03(2) nickel ions per

subunit with an apparent K_d of 21.1(1.7) μM. This contrasts with NiSOD, which shows two binding processes that have been attributed to *cis*- and *trans*-conformers of Pro5, with the pre-formed binding site (*cis*-Pro5) having the higher K_d = 25 nM.[31] The dissociation constant for H15A-SodN, K_d = 20(2) μM (n = 0.5), is similar to SodN, but the nickel binding stoichiometry is half, suggesting an interfacial site formed between two monomers. Analysis of the thermodynamic parameters derived from the binding isotherms also show that the Ni-binding properties of the H15A variant have been altered from those of WT-SodN by the substitution of H15 by Ala. Binding of Ni(II) to H15A-SodN is associated with more favorable enthalpy (ΔH = -21 kcal/mol) and more unfavorable entropy (-TΔS = 14.8 kcal/mol) compared to that of WT-SodN (ΔH = -8.5 kcal/mol, -TΔS = 2.3 kcal/mol) at 25 °C or NiSOD[31] ((ΔH_{cis} = -9.0 kcal/mol, -TΔS_{cis} = -0.9 kcal/mol ΔH_{trans} = -4.1 kcal/mol, -TΔS_{trans} = -4.8 kcal/mol; see **Table S3**). Favorable enthalpy change arises due to strong hydrogen bonding and/or Van der Waals interactions, while favorable entropy changes are associated with desolvation of non-polar groups. The higher enthalpy contributions to nickel binding in H15A-SodN are compensated by higher entropy that give rise to a Gibbs free energy, and hence nickel binding affinity, that is comparable with SodN. Thus,

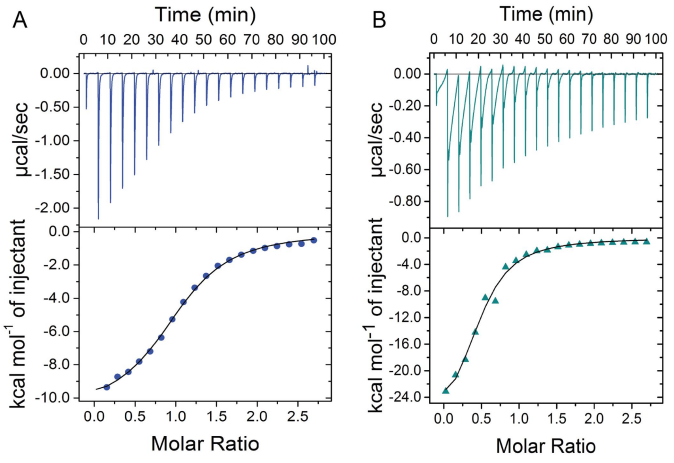

Fig. 2. Ni(II)-binding results for SodN and H15A-SodN using Isothermal Titration Calorimetry (ITC). ITC thermograms (top) and binding isotherms (bottom) for titrations of (a) 0.15 mM of apo-SodN (blue) and (b) 0.15 mM apo H15A-SodN (cyan) with 2 mM Ni(II) in buffer containing 20 mM Tris, 200 mM NaCl, 1 mM TCEP, pH 8.0. One-site binding models were used to fit the isotherms in each case (solid black lines) to give binding stoichiometries of 1.03(2) and 0.47(2) K_d values of 21.1(1.7) μM and 20(2) μM, respectively.

loss of His15 in SodN perturbs the nickel binding energetics in H15A-SodN and reflects a significant role of His15 in the nickel binding process of SodN.

Spectroscopic characterization of the Ni(II)-SodN complex clearly shows that the Ni(II) binding site in the pro-enzyme is distinct from that found in NiSOD, consistent with the observed differences in affinity. The UV-vis spectra of NiSodN, as-isolated NiSOD, and dithionite-reduced NiSOD are compared in **Fig. 3a**. The UV-vis spectrum of NiSodN is similar to apo-SodN (**Fig. S4**) and lacks the S → Ni(III) LMCT absorption characteristic of as-isolated holo-NiSOD (λ_{max} = 372 nm, ε= 7600 $M^{-1}cm^{-1}$) and the higher energy absorptions associated with S → Ni(II) LMCT in dithionite-reduced NiSOD, consistent with a Ni(II) formulation and the absence of thiolate ligation, suggesting that N-terminal processing might be required for thiolate ligation.[32]

Biochemical properties of SodX

SodX is the protease involved in cleaving the N-terminal extension of SodN, and has not previously been overexpressed and purified. The *sodX* gene is found downstream of *sodN* **(Fig. S5a)** in most organisms expressing NiSOD, including *S. coelicolor,* and encodes a polypeptide of 16,157 Da with 146 amino acids that was cloned and overexpressed in *E. coli* **(Figs. S1, S2)**. [25, 33] The purified protein **(Fig. S2, lane 2)** has a +691 Da modification (ESI-MS; 16,848 Da; **Fig. S5b)** that was traced to a likely O-linked-glycosylation (deoxyhexose$(Sulf)_2$), using mass spectroscopic data (Methods) and is monomeric **(Fig. S5c, lane 2)**. The modification occurs in a peptide containing residues 125-142 (likely at Ser128), using mass spectrometry on tryptic peptides and the Expasy Glycomod web-based tool **(Table S2, Fig. S5d-e)**. This result is supported by a modified periodic acid - Schiff (PAS) test and a DTNB (5, 5 – dithio – bis - (2-

nitrobenzoic acid)) test that were both positive and consistent with this modification **(Fig. S5f)**.[34, 35] Despite the glycan modification, SodX showed the expected proteolytic activity at the SodN Ala14-His15 cleavage site (*vide infra*). Further, a sample equilibrated with Chelex resin was found to have no

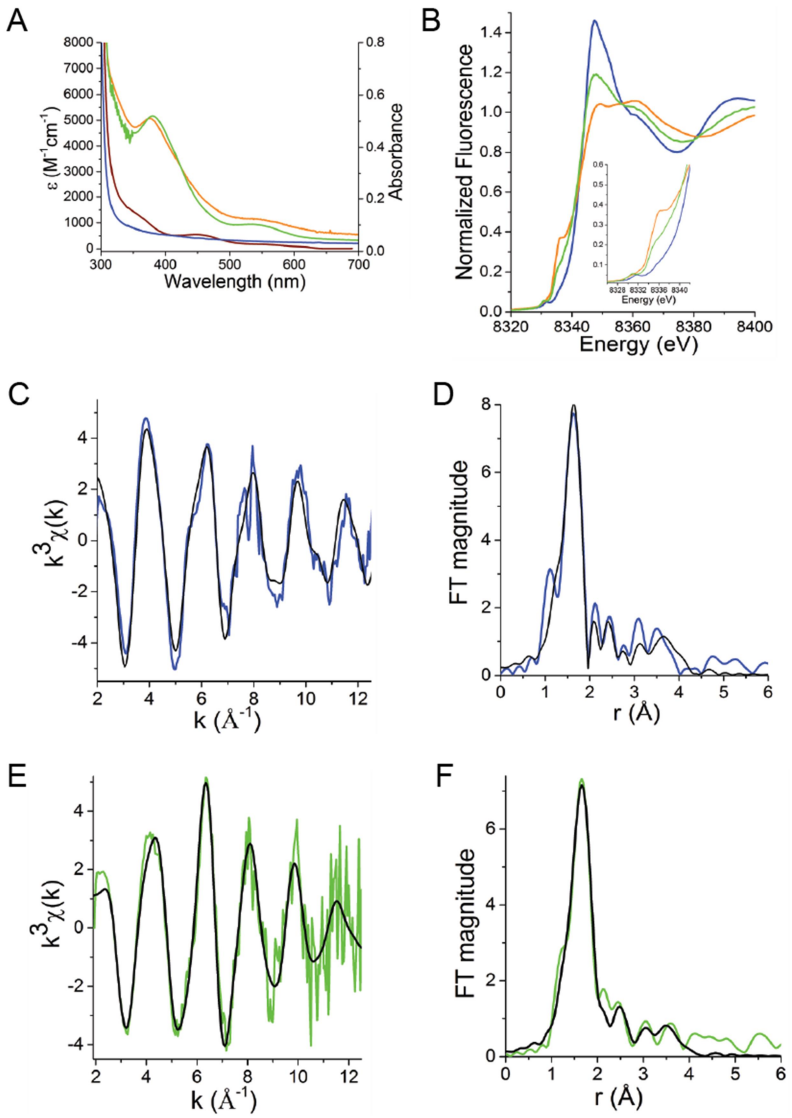

Fig. 3. Spectroscopic characterization of nickel complexes of NiSodN and NiSodN•His. (a) Overlay of the UV-Vis spectra of 100 µM Ni(II)-SodN (blue), as-isolated recombinant NiSOD (orange), dithionite-reduced recombinant NiSOD (wine) plotted vs. ε and for XAS sample of NiSodN•His (green) plotted vs. absorbance. (b) Overlay of the normalized Ni K-edge XANES region of the XAS spectra of Ni-SodN (blue) and NiSodN•His (green) in 50 mM Tris, 200 mM NaBr, pH 8.0 compared with dithionite-reduced NiSOD (orange, Ref.16). Inset: Enlargement of the pre-edge region. (c) k^3-weighted unfiltered EXAFS data for NiSodN (blue) and best fit model from **Table 2** (black). (d) Fourier-transformed EXAFS (k = 2 - 12.5 $Å^{-1}$) data for NiSodN (blue) uncorrected for phase-shifts and the best fit model (black) from **Table 2**. (e) k^3-weighted unfiltered EXAFS data for NiSodN•His (green) and best fit model from **Table 2** (black). (f) Fourier-transformed EXAFS (k = 2 - 12.5 $Å^{-1}$) data for NiSodN•His (green) uncorrected for phase-shifts and the best fit model (black) from **Table 2**.

bound nickel (ICP-OES, Methods), thus excluding the possibility of SodX being a nickel source for NiSOD.

SodX was identified as a serine-lysine protease and a member of the S26A class of proteases based on sequence homology (**Fig. S6**). Consistent with this classification, the proteolysis of SodN is not inhibited by EDTA, ruling out a metalloprotease, (**Fig. S5g),** but is inhibited by acid-denaturation and arylomycin (**Fig. S7a-b & Fig S9a**), which is a specific inhibitor of Ser-Lys proteases.[36-38] This class of serine proteases is typically involved in proteolytic processing of N-terminal signal sequences, *e.g., E. coli* SPaseI, with which SodX has significant sequence homology (**Fig. S6).**[39] Based on the homology and an available structure of inhibitor bound *E. coli* SPaseI (PDB: 1T7D), a model for *S. coelicolor* SodX (without glycan modification) was generated in Pymol using the AlphaFold structure (Q9F3L0) and a peptide (A-HCDLPC) corresponding to the Ni-hook region of SodN **(Fig. 4)** manually positioned in the SodX active site.[40, 41] This model shows the positioning of

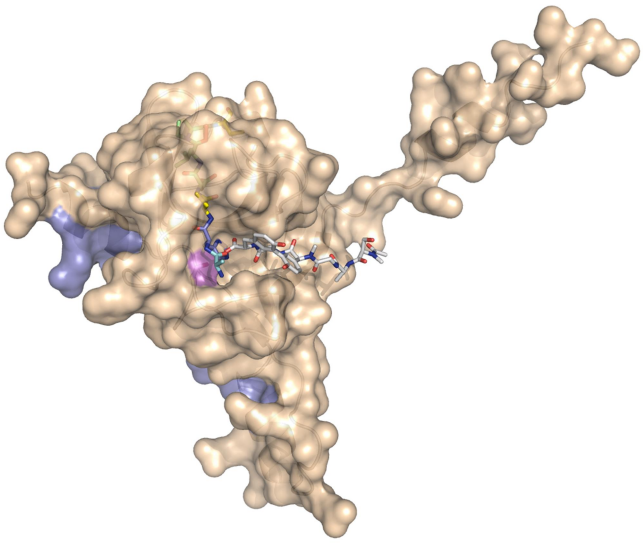

Fig. 4. Homology Model of SodX bound to the SodN peptide substrate. The SodX structure is shown in tan, and represented as a surface. The active site Ser28 nucleophile is colored magenta. The site of the glycan modification (residues 125 – 142) is shown in slate (backside). The inhibitor peptide bound to *E. coli* signal peptidase is shown in grey sticks, with heteroatoms colored, and likely corresponds to the position of the pro- peptide of SodN. The Ni-hook peptide (AHCDLPC; running vertically in the image in stick form, Ala – cyan, His – blue, Cys – yellow, CPL (Cys6-Pro5-Leu4) – green, with heteroatoms colored) was generated in PyMol and manually positioned to highlight the likely binding site with respect to Ser28.

the Ala14-His15 cleavage site of SodN near Ser28, analogous to the catalytic Ser90 in *E. coli* SPaseI. This assignment is consistent with assays of a SodX protein variant, S28A- the glycan modification, SodX showed the expected proteolytic activity at the SodN Ala14-His15 cleavage site (*vide infra*). Further, a sample equilibrated with Chelex resin was found to have no bound nickel (ICP-OES, Methods), thus excluding the possibility of SodX being a nickel source for NiSOD. SodX, which lacks proteolytic activity **(Fig. S7c)** and is also isolated with a similar glycan modification to the WT-SodX (**Fig. S5**).

Proteolytic Processing

SodX can cleave SodN yielding apo-NiSOD. To determine the biochemical requirements for proteolytic processing and Ni insertion into SodN, SodX cleavage of SodN was studied under a variety of conditions (see Methods) and the reaction products were determined by ESI-MS **(Fig. 5)**. Reaction of a mixture containing 40 µM SodN and 40 µM SodX in assay buffer (50 mM Tris, pH 8.0) for 16 h showed the production of WT-apo-NiSOD (equivalent to NΔ14-SodN), consistent with cleavage between Ala14 and His15 **(Fig. 5)**. In addition to the correct SodX cleavage

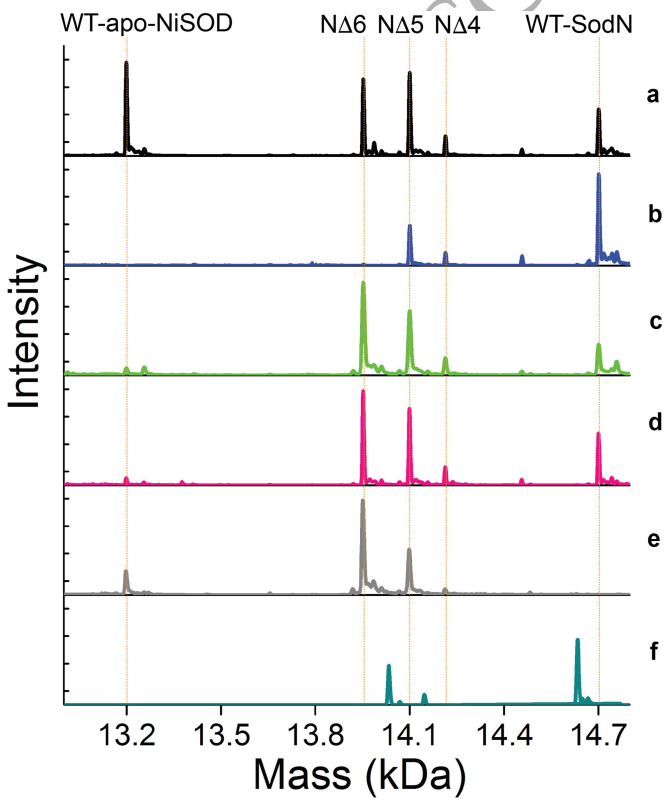

Fig. 5. Deconvoluted ESI-MS spectra of proteolytic reaction mixtures containing SodN, SodX and free metals (Ni, Co, Zn). Reaction mixtures in assay buffer (50 mM Tris•HCl, pH 8.0) containing (a) 40 µM apo-SodN + 40 µM SodX (b) 40 µM SodN incubated with 80 µM $NiCl_2$ (c) 40 µM SodX added to b (d) 40 µM SodX + 40 µM SodN pre-incubated with 80 µM $CoCl_2$ (e) 40 µM SodX + 40 µM SodN pre-incubated with 80 µM $ZnCl_2$. (f) 40 µM apo-H15A-SodN + 40 µM SodX.

product, an NΔ6-SodN species was also present in the SodN - SodX product mixture **(Fig. 5)**, which represents non-specific peptide bond hydrolysis at Phe6-Ala7 **(Fig. S3a,d)**. Other protein species observed in the SodN - SodX product mixtures were unprocessed SodN, NΔ4-SodN, and NΔ5-SodN **(Fig. 5)**, which are all present in isolated samples of SodN **(Fig. S3a,d)** and presumably represent auto-hydrolysis products formed during sample preparation (*vide supra*).

That the resulting apo-NiSOD is functional was confirmed by first adding Ni(II) to the cleavage product mixture using a solution of $NiCl_2$ (150 μM in assay buffer) followed by Chelex treatment to remove loosely bound Ni(II), and then demonstrating activity in the sample using kinetic analysis showing catalysis with pulse radiolytic generation of superoxide **(Fig. 6)**[42] (see Experimental Section for details). Only samples containing correctly processed SodN (apo-NiSOD) by mass spectrometric analysis showed significant catalytic activity. The catalytic removal of superoxide by the reaction product mixtures described gave reaction rates (3.7 x 10^7 $M^{-1}s^{-1}$, based on [Ni]) that were two-orders of magnitude above the spontaneous disproportion of $O_2^{\bullet-}$ at the same pH and similar $O_2^{\bullet-}$ concentration (~ 10^5 $M^{-1}s^{-1}$) [Note: unlike in CuSOD, aquated Ni ions are not

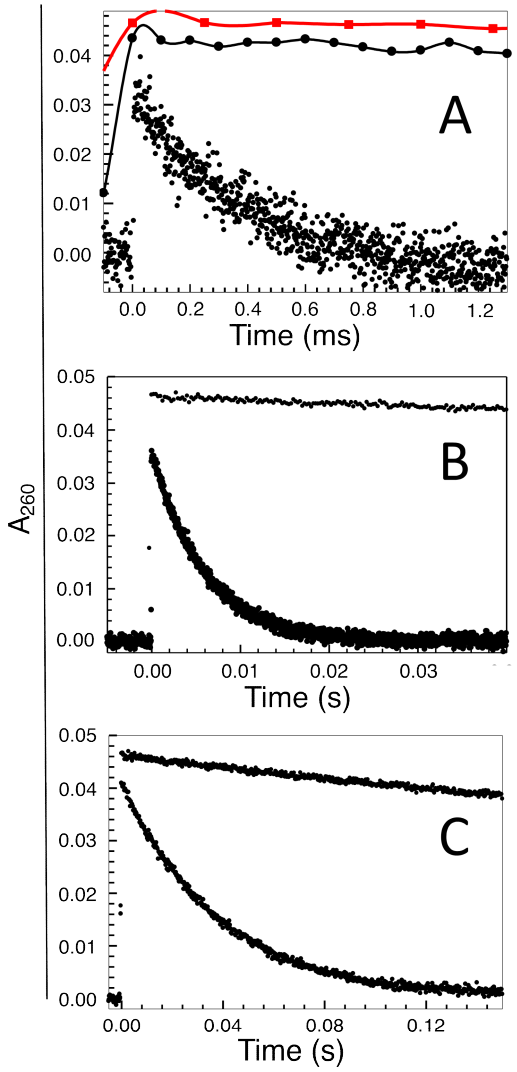

Fig. 6. Activity assessment of NiSOD in cleavage and control experiments using pulse radiolysis. Kinetic traces showing the disappearance of pulse-radiolytically generated superoxide radical by monitoring optical absorbance at 260 nm (ε = 4000 $M^{-1}cm^{-1}$) for buffer (top trace in all panels), which represents the rate for the uncatalyzed bimolecular disproportionation of $O_2^{\bullet-}$), NiSodN (panel A, •-•-•) and catalytic curves (bottom trace in all panels) for WT-NiSOD (Panel A), metal-free cleavage reaction mixture (SodN+SodX) followed by Ni(II) addition (panel B) and cleavage reaction mixture (SodN+Ni+SodX) containing 0.01 mM L-histidine (panel C). The activity was assessed relative to Ni concentrations in each experiment.

catalytically active for the removal of $O_2^{\bullet-}$ but there is no way to confirm that all of the Ni measured in the reaction product mixtures is properly bound exclusively to the apo-NiSOD cleavage product, and therefore the rate is not directly comparable to pure NiSOD.][19]

Metal ions including Ni(II), inhibit *in vitro* cleavage of SodN by SodX. To examine the role of Ni(II) and other metal ions in the cleavage mechanism, the same proteolytic assays as above were performed with Ni(II), Co(II), or Zn(II) added to the cleavage reaction. The reaction products were again detected using ESI-MS and the deconvoluted mass spectra are shown in **Fig. 5**. Addition of $NiCl_2$ (in assay buffer) up to a final concentration of 80 μM to the buffered solution of SodN in the absence of SodX results in a reaction product spectrum **(Fig. 5b)** that is essentially that of purified apo-SodN **(Fig. S3a, top)**, indicating that adding Ni(II) alone does not induce processing. Addition of SodX to preincubated solutions of SodN + $NiCl_2$ (80 μM), $CoCl_2$ (80 μM) or $ZnCl_2$ (80 μM) produces a predominant peak at 13, 954 Da that corresponds to the NΔ6-SodN, a mis-cleaved product **(Fig. 5c-e & Fig S9b)**, with only small amounts of the correct NΔ14 cleavage product. The intensities for the NΔ14 cleavage products are only 8% for Ni- or Co- and 24% for Zn-containing proteolytic assays relative to the metal-free samples. Furthermore, SodN (MW: 14,701 Da) completely disappeared in the Zn-containing proteolytic assay. (A plausible reason for this is the observation of a precipitate in the assay mixture with Zn added. The precipitation of a Zn-SodN complex under the assay conditions might also account for the higher cleavage results for this metal ion, which could result from a loss of Zn from the reaction mixture.) Hence, these proteolytic assays indicate that the presence of metals (Ni, Co or Zn) inhibit the proper proteolysis of the SodN leader sequence.

L-Histidine (but not D-Histidine) restores proper *in vitro* proteolysis in the presence of Ni(II) but not for Co(II). Direct binding of Ni(II) to SodN is unlikely to occur *in vivo*

because of the presence of LMW Ni(II) complexes. These complexes likely necessitate an associative transfer of Ni(II) via a ternary complex for correct enzyme metallation, and would need to be present to explain the prior results from co-expression.[25] L-histidine (L-His) (a known physiological Ni(II) ligand in bacteria), binds Ni in 1:1 (K_{d1} = 15 nM) and 2:1 stoichiometries (K_{d2} = 0.214 μM), with the former–more stable than SodN (K_d = 21μM), but

comparable to *apo*-NiSOD (K_d = 25 nM).[31, 43] Thus, the N-terminally processed protein is expected to be nickelated by the cellular buffered Ni(II) pool (cellular [Ni] ≤ 10^{-12} M and [L-His] = 45 – 180 µM in the cytoplasm of *E.coli* and *Synechocystis*).[7, 8, 44-46] Apo-NiSOD must therefore compete with the buffered Ni(II) pool and might become fully nickelated if Ni is kinetically trapped via coordination of the 4-5 ligands in the active-site Ni hook motif following N-terminal cleavage. The

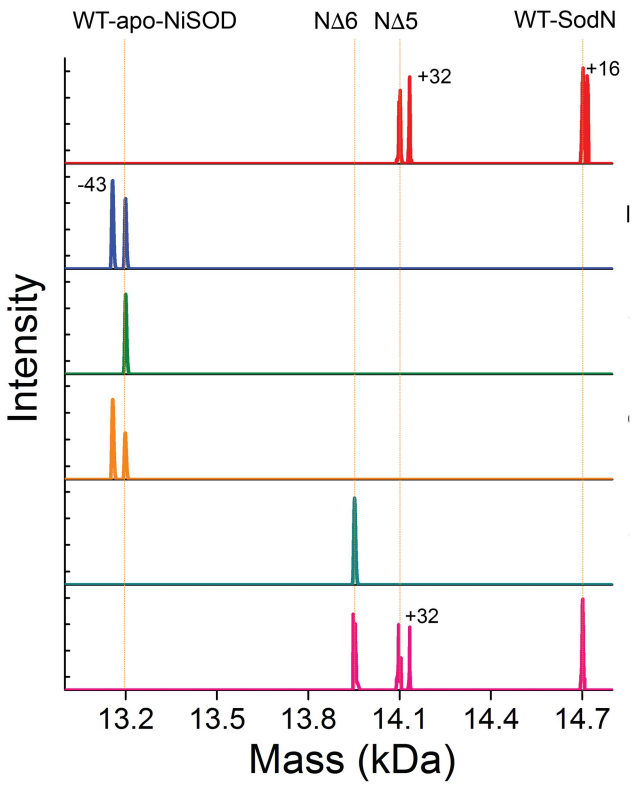

Fig. 7: Deconvoluted ESI- MS traces of proteolysis reaction mixtures (40 µM SodX + 40 µM SodN) in assay buffer (50 mM Tris, 1mM TCEP, pH 8.0) containing L-histidine. (a) with 0.1mM L-histidine, (b) + 80 µM $NiCl_2$ with 0.01 mM L-histidine, (c) + 80 µM $NiCl_2$ with 0.10 mM L-histidine, (d) + 80 µM $NiCl_2$ + 1.0 mM L-histidine, (e) +80 µM $NiCl_2$ with 10.0 mM L-histidine, (f) + 80 µM $CoCl_2$ with 0.10 mM L-histidine.

proteolytic assays were thus repeated with and without 80 μM Ni(II) or Co(II) in the presence of a range of L-His concentrations (0.010, 0.100, 1.0 mM and 10 mM) based on speciation curves **(Fig. S8a)** for a mixture of L-His, apo-SodN, and apo-NiSOD that span the physiological [L-His] in bacterial cytosols (45 – 180 μM in *E.coli* and *Synechocystis*).[7, 8, 44] The results (**Fig. 7** and high resolution data for b-e shown in **Fig. S9c-f**) show that addition of L-His in the absence of Ni(II) inhibits N-terminal processing **(Fig. 7a)**, but adding 0.010, 0.100 or 1.0 mM L-His allowed NΔ14 processing to occur in the presence of 80 μM Ni(II) **(Fig. 7b-d & Fig. S9c-e)**, which is inhibitory in the absence of L-His (**Fig 5b**). The product mixtures from the reactions conducted in the presence of L-His show NiSOD activity that is comparable with samples that were processed in the absence of metals and then nickelated (*vide supra;* specific activity with respect to [Ni] = 1.3 – 3.3 x 10^7 $M^{-1}s^{-1}$) **(Fig. 6)**. Thus, preventing the formation of a Ni(II)-SodN complex that occurs in the absence of L-His enables correct processing by SodX, and indicates that the processed product can be concomitantly nickelated by the buffered Ni pool.

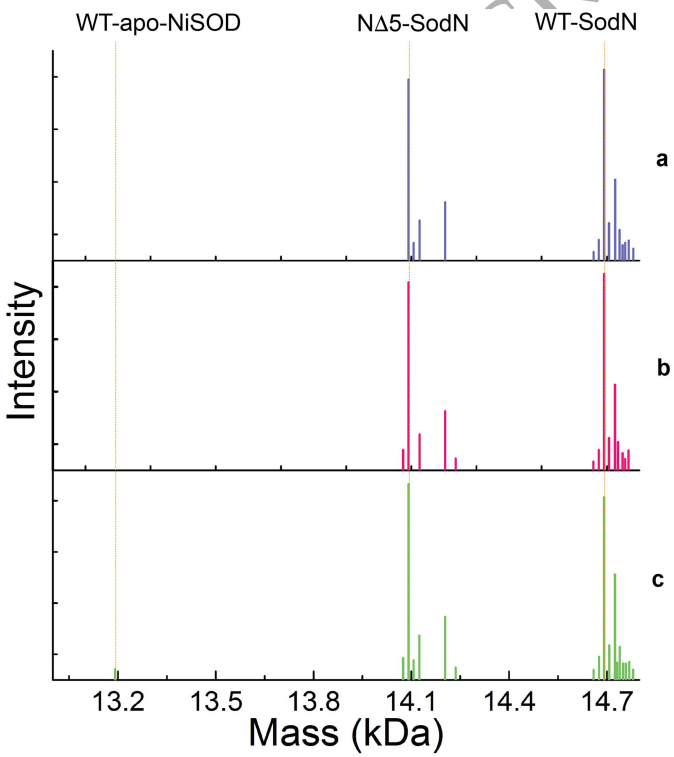

Fig. 8 High-resolution deconvoluted ESI- MS traces of proteolytic reaction mixtures containing SodN, SodX, and Ni at different concentrations of D-histidine. Reaction mixtures containing 40 μM SodX and 40 μM SodN pre-incubated with 80 μM $NiCl_2$ in assay buffer (50 mM Tris•HCl, 1mM TCEP, pH 8.0) with (a) 0.010 mM D-histidine (b) 0.100 mM D-histidine (c) 1.0 mM D-histidine.

The processing assays showing formation of the NΔ14-SodN product with [L-His] = 0.010, 0.100, and 1.0 mM in the presence of 80 μM Ni(II) were repeated using D-His. The results are summarized in **(Fig. 8)** and show that NΔ14 processing is not observed in the presence of 80 μM Ni(II) and 0.010 and 0.100 mM D-His **(Fig. 8a,b)**, and only a trace of the apo-NiSOD product is observed at 1.0 mM D-His **(Fig. 8c)**. This result indicates that the stereochemistry of the Ni(L-His) complex is important in the reaction and is consistent with the formation of a ternary complex between Ni(II), one L-His and either SodN, or a SodN-SodX complex, since SodX does not form a Ni(II) complex by itself. Thus, a ternary complex likely facilitates specific and concomitant nickel insertion into the pre-active site.

At 10 mM L-His and 80 μM Ni(II) the SodX cleavage reaction is once again inhibited **(Fig. 7e, Fig. S9f)**. Under this condition, essentially all the Ni(II) is present as the $Ni(L\text{-}His)_2$ complex, thus promotion of SodN processing by simple chelation of Ni(II) by histidine is questionable. Instead, the apparent inability to process SodN in the presence of $Ni(L\text{-}His)_2$ suggests a possible role for a complex that must compete with the stability of the $Ni(L\text{-}His)_2$, e.g., NiSodN•His, a ternary complex, or a quaternary Ni-His-SodN-SodX complex. Simulation results for the formation of SodN•Ni-His ternary complex with a hypothetical K_d = 0.1μM, tighter than K_d for $Ni(L\text{-}His)_2$ **(Fig. S8b),** further supports the possibility for the formation of such a ternary complex at 0.010 – 1 mM histidine that is present in negligible amounts at 10 mM histidine.

Contrary to the result with 80 μM Ni(II) and 0.1mM L-His, NΔ14 processing is not observed in the presence of 80 μM Co(II) and 0.1 mM L-His (**Fig. 7f**), indicating a degree of nickel specificity for the proteolytic reaction in the presence of L-His.

XAS structural characterization of the SodN Ni sites.

X-ray absorption spectroscopy was used to provide structural information regarding the Ni(II)SodN complex and the same complex formed in the presence of L-His. The XAS reveals a dramatic change in structure that occurs in the presence of L-His that is consistent with the formation of a ternary complex, NiSodN•His.

Ni K-edge XANES: XANES analysis revealed changes in coordination number and geometry of the SodN Ni site that depended on the presence of His in the buffer. The spectra are compared with the spectrum from reduced NiSOD in **Fig. 3b.**[18] All three XANES spectra reveal small pre-edge peaks near 8331 eV that involve promotion of the 1s election into the 3d manifold (1s → 3d). For NiSodN, the area under the 1s → 3d peak is 0.036(2) eV^2, which is consistent with a centrosymmetric distribution of ligands. The spectrum of reduced Ni(II)SOD reveals a second strong and nearly resolved peak near 8336 eV that is attributed to a 1s → $4p_z$ transition that is diagnostic for four-coordinate planar coordination.[47, 48] The spectrum of NiSodN without addition of His shows no evidence of this second feature and the XANES spectrum is therefore characteristic of a six-coordinate complex.[47] Upon addition of His, the resulting NiSodN•His ternary complex reveals a shoulder near 8336 eV that is most consistent with a five-coordinate pyramidal coordination.[47, 49]

While the reduced NiSOD and NiSodN complexes are stable in the X-ray beam, the NiSodN•His complex is not, and reveals exposure-time dependent changes (**Fig. S10a**). First, the edge energy of the Ni K-edge gradually decreases and then stabilizes after the fifth scan (the spectrum shown in **Fig. 3b** is from the last scan of eight), indicating an increase in electron density at the Ni site with increased exposure. The total shift in the edge energy is 0.30 eV. Such

a shift indicates and increase in electron density at the Ni site that is consistent with a reduction of the Ni site (albeit smaller than the ~1eV shift expected for a metal-centered process), an increase in the number of ligands, or a change in ligation of several hard donors for soft-donors (*e.g.,* N/O-donors to S-donors), or a combination of these changes.[47, 50] The presence of a λ_{max} near 380 nm in the UV-vis spectrum (**Fig. 3a**) that has been assigned to a Ni(III)→S LMCT in Ni(III)SOD confirms the formation of some Ni(III)-SOD-like species in the NiSodN•His XAS sample. Thus, the observed edge energy shift is consistent with photoreduction of Ni(III)SodN•His in the beam.

Concomitant with the edge energy shift, the pre-edge features undergo changes in intensity. The peak area associated with 1s→3d feature near 8331 eV gradually decreases from 0.066(12) eV^2 in first scan to 0.038(6) eV^2 in the last scan, while the peak area associated with 1s → $4p_z$ transition increases from 0.023(7) eV^2 in first scan to 0.133(5) eV^2 in the last scan (**Fig. S10b**, inset). Assuming a Ni(II) complex, the 1s → 3d peak area of 0.066 eV^2 is characteristic of a five coordinate complex, while the value of 0.038 is consistent with either a four-coordinate planar or six-coordinate geometry.[50] The increase in absorption associated with the 1s → $4p_z$ transition also suggests that the complex becomes more four-coordinate planar with increased exposure (**Fig. S10a**). Taken together, the edge energy shift and changes in the pre-edge features are consistent with a five-coordinate Ni(III) complex either retaining all the ligands and undergoing a one-electron photoreduction (thus decreasing the number of holes in the 3d manifold), or the loss of a ligand from a five-coordinate pyramidal complex concomitant with a photoreduction. Because the loss of a ligand is inconsistent with a gain of electron density, a simple change in coordination number/geometry of a Ni(II) complex is ruled out. However, it is reasonable that the edge energy shift due to increased electron density upon Ni(III)

photoreduction is moderated by the loss of a ligand. It is noteworthy that the Ni site in NiSOD is five-coordinate in the Ni(III) oxidation state and four-coordinate planar in the Ni(II) complex, consistent with the latter interpretation, however, the Ni site in the enzyme does not undergo a photoreduction in the X-ray beam.[12, 17]

EXAFS: The Ni K-edge EXAFS spectra of NiSodN and NiSodN•His are summarized in **Table 2, Fig. 3c-f and Fig. S10b-d** with details of the analysis summarized in Supporting information and **Tables S5-7.** Analysis of the EXAFS spectrum of NiSodN shows no evidence of S-coordination (max. intensity at k = 6 $Å^{-1}$) and can be fit by six-coordinate models that do not contain S-donor ligands in the primary coordination sphere of the Ni(II) center **(Table S5)**. The Fourier-transformed spectrum does have features that arise from scattering atoms outside the primary coordination sphere that can be fit by including multiple-scattering from histidine imidazole ligands and from ordered C atoms that arise from chelate rings formed by coordination of backbone N-donors, like those found in NiSOD.[18, 51] The best fit **(Fig. 3c-d)**, as judged by R ≤ 5%, decreasing red. χ^2 and acceptable values of σ^2, was obtained for a model that features six N/O-donor ligands and includes one imidazole ligand (likely from His15, *vide infra*). Thus, the Ni(II) site differs from that in the reduced enzyme in terms of coordination number/geometry, the ligand environment, and consequently, the spin state of Ni(II), which is low-spin for NiSOD but high-spin here because of the six-coordinate site.

In contrast to the EXAFS obtained for NiSodN, the EXAFS for the NiSodN•His samples show a clear beat pattern maximizing at a k = 6 $Å^{-1}$, and cannot be modeled without including at least one S-donor ligand (**Table 2 and Fig. 3e, f**). Because of the photosensitivity in the beam

(**Fig. S10a**), the EXAFS for NiSodN•His corresponding to the first and last of these scans were analyzed separately (**Table S6, S7**). Since these are single scans, the analysis is more limited relative to NiSodN because of poorer signal:noise. The best fit models for the EXAFS of the NiSodN•His complex in the final scan are consistent with four- or five- coordinate nickel sites with 2-3N/O-donors at ~2.0 Å, 1 imidazole at ~2.0 Å, and at least one S-donor at ~2.2 Å (**Fig. 3e-f**): $[Ni(N/O)_{2\text{-}3}(Im)S]$. These Ni-donor atom distances are systematically shorter than for NiSodN (**Table 2**), and are typical of low-spin Ni(II) complexes, particularly the ~2.2 Å Ni-S distance.[47, 52] Thus, the change in geometry also results in a large change in electronic structure, as all octahedral Ni(II) complexes are high-spin.

Inclusion of a second long S-donor at 2.6 Å (**Fig. S10b**) to give a five-coordinate model that is more consistent with the XANES analysis, $[Ni(N/O)_2(Im)S_2]$, leads to a highly disordered long S scattering atom. However, the weakness of a long bond might give rise to considerable disorder, so this model remains a possibility. Cys16 and/or Cys20 are the likely candidates for S-coordination, while the imidazole ligand could be His15, or provided by the L-Histidine in the medium.

Similar to the final scan, the best fit model for the EXAFS of NiSodN•His complex for the first scan is also either a four- or five- coordinate low spin Ni(II) site with 2-3 N/O- donors at 2.04 Å, 1 imidazole at 1.96 Å and at least one S-donor at 2.20-2.23 Å. Again, the addition of a second long and disordered S-donor at ~2.6 Å is a possibility (**Fig. S10c-d, Table S7**). That the coordination environment of the nickel center in the first and last scans of the ternary complex of NiSodN•His remains similar at He temperatures is more consistent with a photoreduction without an accompanying ligand change, but the EXAFS data could be dominated by a single

Ni(II) site that is not affected on average by the photoreduction of a smaller amount Ni(III) that produces the same Ni(II) center.

DISCUSSION

This work addresses several facets of the mechanism of the maturation of NiSOD (Scheme 1). The cleavage of SodN by SodX in the absence of nickel and the inhibition of the proteolysis observed upon the addition of Ni(II) ions contrast with the results obtained from co-expression of SodN and SodX *in vivo* that showed increased NiSOD activity with increasing Ni(II) concentration.[25] The inhibition by Ni(II) in the *in vitro* reaction was overcome by the addition of L-His, a known component of the LMW cytoplasmic labile Ni(II) pool[3], demonstrating a role for this cytoplasmic ligand at physiologically relevant concentrations in the maturation of NiSOD from SodN in the presence of Ni(II), and providing an explanation for the difference for the role of Ni in *in-vivo* and *in vitro* maturation.

L-His-dependent processing was shown to be Ni(II)-specific. Further, L-His was found to inhibit the metal-free cleavage of SodN by SodX. Thus, under cellular conditions (45 – 180 μM histidine), cleavage would only proceed in the presence of Ni(II), linking the *in vitro* processing of SodN with the *in vivo* experiment.[25]

In vivo, cytosolic nickel is buffered to 10^{-12} M.[45] The importance of competition with LMW Ni complexes, specifically L-His, has been demonstrated for Ni(II)-responsive bacterial metalloregulators, such as InrS, which have much tighter Ni(II) binding (InrS $K_d \sim 0.5$ nM) than reported here for SodN ($K_d = 21$ μM) and apo-NiSOD (K_d = ~25 nM for the conformer with *cis*-Pro5.[7, 31] Taking the Ni(II) affinities of SodN and apo-NiSOD at face value, the thermodynamic competition between Ni(II) in the buffered cellular nickel pool and SodN is negligible, and the formation of the His-free complex, NiSodN, is an artifact of the *in vitro* preparation. While apo-NiSOD could effectively compete for Ni with the LMW Ni(II)His pool after N-terminal processing, and kinetically trapping the metal through Ni-hook formation, a simple competition between SodN and a buffered pool of Ni(II) cannot be responsible for both restoring N-terminal processing *and* nickelation. Our observations support a process in which SodX recognizes a specific ternary complex, NiSodN•L-His, that enables site-specific cleavage of Ala14-His15. Precedence for protein recognition of specific complexes of L-His, and not D-His, has been demonstrated in bacterial trans-membrane import of Ni(II) via the bacterial NikA(BCDE) transporter system.[8, 9, 53]

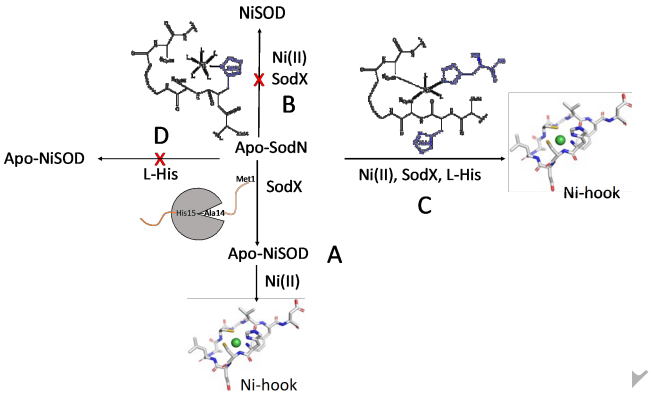

Scheme 1: Scheme summarizing the *in vitro* N-terminal processing of SodN by SodX. Pathway A indicates that cleavage of SodN by SodX produces apo-NiSOD that can subsequently be nickelated to give active NiSOD. Pathway B indicates that in the presence of Ni(II) SodX does not cleave SodN to give NiSOD, likely due to the formation of a Ni(II) complex involving coordination of His15 at the cleavage site (see text). Pathway C indicates that the addition of L-His allows SodX cleavage of SodN in the presence of Ni(II), which occurs via a unique SodN•SodX•L-His ternary Ni complex (see text). Pathway D illustrates that cleavage in the absence of Ni(II) is inhibited by L-His.

Ternary complex formation has important effects on Ni-binding to SodN. In the absence of L-His, SodN forms a high-spin, six-coordinate Ni(II) complex (from XAS). This site is distinct from that found in NiSOD, particularly in regards to the coordination number (six) and absence of thiolate coordination in the nickel site. In NiSOD, binding of sulfurs (from Cys2 and Cys6) is an 'all or none' phenomenon, meaning that both sulfurs are required to support the native low-spin Ni(II) configuration.[54] High-spin, six-coordinate mono-thiolate nickel complexes are rare and feature very long (weak) Ni-S bonds (2.46-2.54 Å), such as those found in Ni(tren)(1,3-dtsq)(H_2O), Ni(tren)(1,3-dtsq)(H_2O), and Ni-RcnR.[54-56] In fact, prior to forming the 'Ni-hook' feature, it is not sterically possible to coordinate Ni(II) to both Cys residues and to His15.[12] Thus, SodN seems to have evolved to prevent Cys coordination in any complex employing His15 as a ligand.

Ternary complex formation also provides insights into the cleavage mechanism and its inhibition by Ni(II) in the absence of L-His. With the exception of the N-terminal amine, the Ni-hook ligands in apo-NiSOD (HCXXC) are available in SodN and lie in the protein binding site of SodX (Fig. 4). Nonetheless, EXAFS analysis of NiSodN shows that Cys16 and Cys20 are not Ni ligands and is consistent with the binding of His15 (**Table S5, Fig. 3b,c**). The His coordination in NiSodN (EXAFS) and the requirement for His15 in both SodX cleavage and coordination of Ni(II), suggests that binding Ni at His15 might interfere with the proper recognition of the cleavage site, or with cleavage by SodX. One possible role for L-His in N-terminal processing by SodX is to compete for Ni(II) coordination with His15, thus allowing a ternary complex to form with L-His, Cys16 and/or Cys20 as ligands. Indeed, the analysis of XAS data for the NiSodN•His ternary complex is consistent with a four- or five-coordinate low-spin Ni(II) complex with histidine and cysteine ligation. This complex is also consistent with 1:1

Ni(II): L-His stoichiometry and places Ni(II) in the nascent binding site, but away from the Ala14-His15 cleavage site in SodN, eliminating interference with SodX. The complex may also assist in 'Ni-hook' formation after processing and supply Ni(II) for the formation of the NiSOD active site via displacement of the L-His ligand by the chelate formed with the N-terminal amine and His1 imidazole. Further, the formation of NiSodN•His is important to recognition of the SodN cleavage site by SodX, since a D-His complex inhibits N-terminal processing and processing in the presence of Co(II) is not rescued by L-His.

Recognition of a nickel complex of a pro-protein by its cognate protease is a feature of [Ni, Fe]-H_2ase maturation.[26] The heterometallic active site of [Ni, Fe]-H_2ase is buried inside the large subunit, which is also expressed as a pro-protein and requires C-terminal processing[27]. The proteolytic processing of [Ni, Fe]-H_2ase large subunit is dependent on the sequential insertion of active site metals – Fe insertion first, along with the non-protein CN^- and CO ligands, involving the HypCDEF accessory proteins, followed Ni insertion by HypA and HypB.[26, 27] Once the metals are inserted into the pre-active site, a cognate aspartyl endopeptidase (*e.g.*, HycI, for the hydrogenase 3 large subunit, HycE) recognizes the C-terminal extension and cleaves it, which then facilitates the docking of a small subunit containing Fe-S clusters and completes the maturation of [Ni,Fe]-H_2ase.[26, 27, 57] Metal specificity is conferred by the sequential incorporation of the ligands. Ni(II) cannot be bound to the pro-enzyme prior to the construction of the Fe site, and substitution of other metals (*e.g.,* Zn(II)) for Ni(II) prevents C-terminal processing.[58-60] In the case of NiSOD, a ternary complex formed between SodN, L-His, and Ni(II) provides specificity.

CONCLUSION

The mechanism of NiSOD maturation discussed here raises the possibility that the role of the N-terminal extension in SodN is to ensure fidelity of the Ni site formation in conjunction with cleavage by SodX. The LMW His complexes work to fulfill many of the functions of a metallochaperone, such as preventing the formation of off-pathway protein complexes and facilitating high-fidelity nickel insertion in the active site. Further, by forming a ternary complex with SodN that is potentially recognized by SodX, such a complex also provides a potential mechanism for selective incorporation of Ni(II) in to apo-NiSOD, in analogy with the maturation of Ni,Fe-H_2ase.

EXPERIMENTAL SECTION

Gene Cloning, Mutagenesis and SodN, SodX Protein Expression, and Purification

The WT-*sodN* gene from *S. coelicolor* (**Fig. S1**) in the pET3a plasmid carrying resistance gene for ampicillin for selection was generously provided by J. H. Roe from Seoul National University. The pET3a-SodN plasmid was used to transform BL21(DE3) plysS cells carrying resistance gene for chloramphenicol. The transformed cells were grown in 0.5 mL Luria Bertini (LB) media in 5 ml tubes at 37°C for 1 hour and aliquots were plated on agar plates containing the chloramphenicol and ampicillin antibiotics. A single colony was picked and grown overnight in LB media (200 mL) supplemented with chloramphenicol and ampicillin at 37^{o}C with shaking at 200 rpm. A 10 mL aliquot of the overnight culture was added to 1 L of the pre-warmed fresh LB media, grown to an OD_{600} of 0.6-0.8, and then induced with 0.8 mM of isopropyl – β-D-1-

thiogalactopyranoside for 3-4 hours at 37°C. Cells were harvested by centrifugation at 8000 rpm for 15 min and frozen at -80°C.

Site-directed mutagenesis was used to introduce Ala substitutions at His15 of SodN. The pET3a-SodN vector was used as the template DNA for the single point mutations using polymerase chain reaction (PCR) and PCR primers (listed in **Table S1**) were designed to incorporate the desired mutations. For each 50 μL volume of PCR reaction mixture, 0.5 μM (25 picomoles) of each primer was used for 2 ng of template DNA. Successful PCR amplifications were determined using 0.8% agarose gel and the amplicons were subsequently digested with *Dpn*I for 1 h at 37°C to remove any methylated template DNA. The digested PCR mixture was then used to transform DH5α competent cells carrying no resistance gene for selection, and the cells were plated on LB-agar media supplemented with 100 mg/mL ampicillin (Fisher Scientific), followed by incubation at 37°C for 12-16 hours. Single colonies from the plates were grown to saturation in 5ml LB-miller broth supplemented with ampicillin at 37°C. Cells were pelleted at 13,000 g for 5 minutes and the plasmids were isolated using GeneJET plasmid miniprep kit (Thermo Fisher Scientific). Gene sequencing (Genewiz, Inc.) confirmed the successful mutations.

The harvested cells were thawed at 37°C and re-suspended in Buffer A (50 mM Tris•HCl, 1mM TCEP, pH 8.8). DNase I solution (100 μL of 10 mg/ml DNase, 10 mM $MgCl_2$, 20 mM Tris, pH 7.5 and 40% glycerol) and 380 μL of 0.2 M PMSF were added and incubated at 37°C until the viscosity of the solution was sufficiently reduced. The cells were then sonicated using SONICS (Vibracell) using 3s pulses at 40% power with a 12 s interval to further lyse the cells. Lysed cells were centrifuged at 10,000 rpm for 45 minutes at 4°C, and the clear supernatant was used for protein purification.

All chromatographic purification steps were carried out using AKTA-FPLC system (Amersham Biosciences). The supernatant was loaded onto a pre-equilibrated Q-Sepharose column (GE Health Sciences) at a rate of 2.00 ml/min with buffer A. Once the absorbance returned to baseline value, the protein was eluted with a linear gradient of Buffer B (50 mM Tris, 1 mM TCEP, 1 M NaCl, pH 8.8). All the fractions containing protein were collected and analyzed using SDS-PAGE. Fractions containing SodN (MW 14,702 kDa) were pooled and buffer-exchanged against Buffer C (50 mM HEPES, 1 mM TCEP, pH 7.0) using a PD-10 column (GE Healthcare) and loaded on a pre-equilibrated SP-Sepharose column at a rate of 2.00 ml/min. The column was washed with five column volumes of Buffer C and protein was eluted with Buffer C containing 1 M NaCl. The purity of collected protein fractions were analyzed by SDS-PAGE and the fractions containing SodN were pooled and concentrated (**Fig. S2**, lane 4). The yield of protein using this purification method was 5-7 mg/L as determined from the protein concentrations using the absorbance at 280 nm and a theoretical extinction coefficient of 17,085 $M^{-1}cm^{-1}$ obtained from web-based Expasy Protein Parameters tool. EDTA (up to a final concentration of 1 mM) and 10 % glycerol were added to the concentrated protein stock, which was stored frozen at -20^{o}C until needed. The protein expression for H15A SodN was found similar to that of WT-SodN and was purified as described for SodN.

sodX from genomic DNA of *S. coelicolor* (obtained from Wellcome Sanger Institute, United Kingdom) was amplified using PCR with forward and reverse primers (*sodX-1*) given in **Table S1**. The purified PCR product was obtained from a 1% agarose gel and digested with BspEI and XhoI to create overhangs complementary to the pET23bSUMO vector. The insert was ligated to pET23bSUMO vector using Quick Ligase (New England Biolabs) and the ligated DNA was used to transform GC10 cells, which were then plated on LB-agar media containing

100 mg/ml ampicillin for selection, and incubated overnight at 37°C. Single colonies were picked and grown overnight in 2 mL LB-Amp media at 37°C and the pET23bSUMO-SodX plasmid was then extracted using Thermo Scientific miniprep Kit. The plasmid was further digested using XmaI, AvaI, BstII, NheI, and ApaLI to confirm the insertion of *sodX* at the correct position of the vector. The gene sequence was confirmed by DNA sequencing (IDT, Inc.).

The pET23bSUMO-SodX plasmid containing chloramphenicol and ampicillin resistance genes for selection was used to transform BL21(DE3) plysS cells. A single colony was picked and grown overnight in LB media supplemented with both antibiotics at 37°C with shaking at 200 rpm. A 10 mL aliquot of the overnight culture was added to per liter of the pre-warmed fresh LB media, and then grown to an OD_{600} of 0.6-0.8, followed by induction with 0.95 mM of isopropyl – β-D-1-thiogalactopyranoside solution and incubation for additional 3 hours at 37°C. Cells were harvested by centrifugation at 8000 rpm for 15 min and frozen at -80 °C. However, the protein overexpressed from this construct failed to bind to the His-trap column and hence could not be purified using nickel affinity chromatography. Therefore, *sodX* was sub-cloned onto the pET22b vector as follows.

The *sodX* gene from M108 forward was cloned out of the pET23bSUMO plasmid using PCR amplification with forward and reverse primers (*sodX-2*) as given in **Table S1**. The purified PCR product was obtained from an 0.8% agarose gel. The product was digested with NdeI and XhoI to create overhangs complementary to the pET22b vector. The insert was ligated to the pET-22b vector using ligase, and DH5α *E. coli* cells were transformed with the pET-22b vector containing the SodX gene (pET-22b/SodX). The DH5α cells were grown in 0.5 mL LB media at 37°C for 1 hour and aliquots of the culture were plated on LB media containing 100 mg/ml of

ampicillin and incubated overnight at 37°C. Single colonies were picked and grown overnight in 5mL LB-Amp media at 37°C for pET22b-SodX plasmid extraction using the GeneJET plasmid miniprep Kit (Thermo Fisher). The gene sequence was confirmed by Genewiz, Inc. (**Fig. S1**). The pET22b-SodX plasmid was then used to transform BL21 (DE3) plysS cells. The transformed cells were grown in 0.5 mL LB media in 5 ml tubes at 37°C for 1 hour and aliquots were plated on agar plates containing the chloramphenicol and ampicillin antibiotics. A 10 mL aliquot per liter of media of the overnight culture was added to pre-warmed fresh LB media, grown to an OD_{600} of 0.6-0.8 and then induced with 0.95 mM of isopropyl – β-D-1-thiogalactopyranoside for 3 hours at 37°C. Cells were harvested by centrifugation at 8000 rpm for 15 min and frozen at -80°C for storage.

Site-directed mutagenesis was used to introduce Ala substitutions at Ser28 of SodX. The pET 22b-sodX plasmid was used as the template DNA for the single point mutations using polymerase chain reaction (PCR) and PCR primers (listed in **Table S1**) were designed to incorporate the desired mutations. Ser28ASodX plasmid was obtained using the PCR protocol for His15ASodN as described above. Gene sequencing (Genewiz, Inc.) confirmed the successful mutations. The protein expression for S28A-SodX was found similar to WT-SodX,

The harvested cells were thawed at 37°C and re-suspended in Buffer A (50 mM HEPES, pH 8.5). 100 µL of DNase I solution (containing 10 mg/ml DNase, 10 mM $MgCl_2$, 20 mM Tris, pH 7.5 and 40 % glycerol) was added and the mixture was incubated at 37°C until the viscosity of the solution was sufficiently reduced. The cells were then sonicated with SONICS (Vibracell) using 3s pulses at 40 % power with a 12s interval to further lyse the cells. Lysed cells were then centrifuged at 10,000 rpm for 45 minutes at 4°C and the supernatant was filtered using a 0.22 µM syringe filter. The clear filtrate was used for protein purification.

All chromatographic purification steps were carried out using AKTA-FPLC system (Amersham Biosciences). The filtrate was loaded onto an SP-Sepharose column (GE Health Sciences) at a rate of 3.00 ml/min with buffer A. Once the absorbance returned to baseline value, the protein was eluted with a linear gradient of Buffer B (50 mM HEPES, 1 M NaCl, pH 8.5). All the fractions containing protein were collected and analyzed using SDS-PAGE. Fractions containing pure SodX (MW 16,157 Da) were pooled (**Fig. S2**, lane 2), and the protein concentration was determined using its theoretical molar extinction coefficient value of 24,960 M^{-1} cm^{-1} determined using web-based Expasy Protein Parameters tool (https://web.expasy.org/protparam/). Portions (200 µl) of the 150 µM purified protein solution were aliquoted and frozen at -20^{o}C until used for experiments. S28A-SodX variant was purified similarly to that of WT-SodX as described here.

Mass Spectrometry for Protein Characterizations

Molecular weights of all purified proteins were determined using LC-MS, where the purified protein samples were passed through a C-8 BioBasic column (Thermo Scientific) that was pre-equilibrated with solution A (0.1% formic acid in water). The protein samples were eluted using 95% of solution B (0.1% formic acid in acetonitrile) and injected into an AB Sciex QStar XL ESI-Q- TOF mass spectrometer, which was previously calibrated with PfHA.

SodX – MS/MS: For Collision Induced Dissociation (CID) on SodX, the protein was diluted in 50% MeOH solution and then directly injected into Synapt G2Si HDMS. The parent peak with m/z of 1296 was used for MS/MS. Collision-Induced-Dissociation (CID)-MS (**Fig. S5d**) performed on SodX confirmed the absence of any extra residues at the C- or N-terminus and eliminated the possibility of modification at the terminals.

SodX - LC/MS/MS: Purified SodX was buffer exchanged in 50 mM NH_4HCO_3. A portion of this sample was diluted to a final concentration of 25 µM which was digested with 20 µg trypsin (Sigma Aldrich) in 50 mM NH_4HCO_3 and incubated for 16 h at 37^{o}C. The reaction was stopped by addition of 10% formic acid. The tryptic digest was passed through nano-LC (Easy nLC 1000) pre-equilibrated with solution A (0.1% formic acid in water) and eluted using 95% solution B (0.1% formic acid in acetonitrile). The m/z of peptides obtained after LC-MS/MS of the tryptic digest of SodX are shown in **Table S2**. MS/MS spectra (**Fig. S5e**) with high intensity in each peptide of the protein were selected from 800 – 6000 m/z and fed into the Expasy GlycoMod tool(https://web.expasy.org/glycomod/), which generated theoretical O-glycosylated modification of varying masses. One such predicted modification corresponded to the difference in mass observed for SodX (Δm = + 691.5 Da).

SEC-MALS

A stock of purified protein samples (apo-NiSOD and apo-SodN or WT-SodX) was buffer exchanged in gel filtration (GF) buffer (50 mM Tris, 200 mM NaCl, pH 8.0). A TSKgel G2000SWxL column (Tosoh Bioscience) was attached to Agilent HPLC system that was coupled to DAWN HELEOS II light scattering detector (Wyatt Technology) and the Optilab T-rEX refractometer (Wyatt Technology). The system was equilibrated with GF buffer at 0.5 mL/min and experiments were performed at 25^{o}C. 25 µL aliquots of 50 µM apo-NiSOD, apo-SodN protein solution were injected for SEC-MALS analysis at a flow rate of 1.5 mL/min. Eluted proteins were monitored by multiple components of the instrument: UV at 280 nm, light scattering at 664 nm with detectors at multiple angles (13 - 157.8^{o}) and refractive index at 658 nm. Each chromatogram was processed using Astra 6 software package (Wyatt Technology) as described previously.[61] The absolute mass of Bovine Serum Albumin (BSA, expected 66.5

kDa, SEC-MALS 64.7 kDa) was used to calibrate the system and the software. Based on the MALS data, the apparent molecular masses of apo-SodN, apo-SOD and WT-SodX were calculated to be 95.38 ± 0.04 kDa, 89.69 ± 0.05 kDa, and 16.8 ± 0.1 kDa respectively (**Fig. S3b and Fig. S5c**), values that are consistent with a homohexameric quaternary structure for SodN.

Circular Dichroism

The purified proteins (apo-NiSOD and apo-SodN) were buffer exchanged in CD buffer (25 mM Tris, 100 mM NaCl, pH 8.0). The protein stock solutions were transferred to an anaerobic chamber (Coy), reduced with 5 equivalents of DTT and incubated for 1 hour at room temperature. The reduced protein samples were then buffer exchanged in CD buffer, followed by the addition of three equivalents of $NiCl_2$ and incubation for an additional three hours. Chelex beads were added to remove excess metal, and the metallated proteins (holo-NiSOD and holo-SodN) were buffer exchanged for an additional three times with CD buffer. The metal content of the samples were checked using ICP-OES. 20 μM of each these protein samples (apo-NiSOD, holo-NiSOD, apo-SodN, holo-SodN) was used to obtain their CD spectrum (**Fig. S3c**) on Jasco J-1500 Circular Dichroism Spectrophotometer.

Isothermal Titration Calorimetry

Isothermal titration calorimetry (ITC) was used to measure the heat released by Ni-binding to apo-SodN (WT- or H15A-) proteins using an Auto-ITC200 model microcalorimeter (Microcal/Malvern). The instrument has a cell volume of 200 μL and a syringe volume of 40 μL, which were filled by robotic arms from plates stored at 4℃ prior to the start of the experiment. All titrations were performed in ITC Buffer (20 mM Tris, 1 mM TCEP, 200 mM NaCl, pH 8.0) at 25℃ with the reference cell filled with water. A stock of purified proteins (SodN or its variants) were buffer exchanged in ITC buffer (20 mM Tris, 1 mM TCEP, 200 mM NaCl, pH

8.0) using Amicon Ultra – 0.5 mL centrifugal filters with 3-kDa MWCO pre-equilibrated with ITC Buffer and then diluted to 150 μM for titration immediately before the ITC experiments. $NiCl_2$ was dissolved in MilliQ water from a 10 mM stock solution and its exact concentration was checked by ICP-OES. An aliquot of this solution was diluted in ITC Buffer to a final concentration of 2.0 mM and was used for titrations.

For each ITC experiment, 20 injections were made from the syringe into the cell and the change in heat was monitored by the instrument. The initial injection contained only 0.4 μL and was used to minimize the equilibration artifacts sometimes observed with the first injection and was not included in fitting the data. All subsequent injections at 2.0 μL each were used for fitting the titration curve in each experiment. For titration of SodN (WT- or variants) with $NiCl_2$, the spacing between injections were set to 300 sec. Experimental titrations were accompanied by corresponding reference/control titrations of $NiCl_2$ into ITC Buffer in the cell, the resulting heats of which were used to establish the corresponding baseline corrections used for fitting the ΔH data. Experimental titrations were performed thrice using separately prepared proteins, and each replicate produced similar results.

The resulting data were fitted using the MicroCal analysis module in Origin7.0. First, the heat released from titration experiments were baseline corrected and then integrated to produce the corresponding ΔH curve. The ΔH curve for each experiment was corrected by subtracting the average ΔH from the reference titration. The ΔH curve was fitted with the OneSites model to find the apparent K_a (multiple fitting models were attempted for each set of experimental data and in each case the OneSites model produced the best χ^2 value). The apparent k_d values reported are the inverse of the k_a values obtained from each fit.

UV-Vis Spectroscopy

A stock solution of purified SodN was buffer exchanged in buffer C (containing 50 mM Tris, 1 mM TCEP, 200 mM NaCl, pH 8.0). A 120 µL sample of 100 µM apo-SodN in Buffer C was scanned from 250 nm to 1100 nm using an Agilent 8453 Diode-array spectrophotometer. For nickel-bound SodN, the purified and buffered exchanged apo-protein solutions were incubated with an equivalent amount of nickel for 15 minutes and scanned similarly.

For characterization of the XAS sample. 20 µL of the sample of NiSodN•His was diluted to 110 µL in Buffer X (50 mM Tris, 200 mM NaBr, 0.1 mM L-Histidine, pH 8.0) and the sample was scanned from 200 nm to 800 nm using a Cary-UV-Visible spectrophotometer.

SodX Characterization

1. PAS test: A periodic acid Schiff test with slight modification from the microtiter-based protocols was done on SodX or S28A-SodX. Briefly, 25 µL of 59.35 µM (1 mg/mL) of SodX or S28A-SodX, was oxidized with 120 µL of 0.06% periodate solution made in 7% acetic acid, and the mixture was incubated for 1.5 hours. 100 µL of the Schiff's reagent was then added to the mixture and incubated for additional 30 minutes.[34, 62] Absorbance for these samples were recorded from 350 – 750nm (**Fig. S5f**).

2. Sulfhydryl assay: A sulfhydryl assay with 5,5'-Dithiobis-(2-Nitrobenzoic acid) (DTNB) was performed on SodX (WT and S28A variant) using the standard protocol (Thermo Scientific). Briefly, a stock of DTNB solution was made by dissolving 26.34 mg in 1 mL reaction buffer (0.1 mM sodium phosphate, 1mM EDTA, pH 8.0). A set of cysteine standard solutions (0 mM - 1.5 mM) were made using Cysteine hydrochloride in reaction buffer. The protein stock samples were diluted to 50 µM. 250 µl of cysteine standard or protein sample was

added to a solution containing 50 µl DTNB solution and 2.5 mL reaction buffer. The mixture was incubated at room temperature for 15 minutes and the absorbance of each solution was measured at 412 nm using Agilent 8453 Diode-array spectrophotometer. A standard curve was made using the absorbance values of the standards and the concentration of the protein sample was obtained from this curve.

3. Homology Model: The *S. coelicolor* SodX model structure coordinates (Q9F3L0) were downloaded from uniprot.org. The model structure was aligned in Pymol to the *E. coli* signal peptidase (1T7D[40]) using all atoms. A heptapeptide (A-HCDLPC) corresponding to the N-terminus of apo-SodN (and including the last residue of the pro-sequence) was built in Pymol and manually positioned in the active site of SodX.

4. Inactivation of SodX: Inhibition of proteolytic activity of SodX was tested with EDTA, acid denaturation and an SPaseI inhibitor compound 9, Arylomycin[38] obtained from The Scripps Research Institute. To rule out metalloprotease, DTT-reduced SodN (40 µM) in 5 mM EDTA containing assay buffer M1 (50 mM Tris, pH 8.0) was incubated with WT-SodX (40 µM) at 30 ^{o}C for 16 hours. The sample was then passed through a C-8 BioBasic column (Thermo Scientific) that was pre-equilibrated with solution A (0.1% formic acid in water). The protein samples were eluted using 95% of solution B (0.1% formic acid in acetonitrile) and injected into an AB Sciex QStar XL ESI-Q- TOF mass spectrometer, which was previously calibrated with PfHA.

Similarly, for acid-denaturation, a stock of purified WT-SodX was diluted to 100 µM in assay buffer M2 containing 1M HCl and incubated for at least 15 minutes prior to setting up the proteolytic assay described above.

For inhibition with Arylomycin (stock concentration, 10 mg/ml), a stock of purified WT-SodX (1.8 mg/ml) was diluted to 1mg/ml and incubated with the inhibitor (1mg/ml final concentration). An aliquot from this sample was then used to conduct the proteolytic assay where the final concentration of SodX used was 0.674 mg/ml (or 40 μM).

In Vitro Processing assays

All metal stock solutions were made in deionized water obtained from a Milli-Q (EMD Millipore) water purifier, and the metal content was quantified using ICP-OES (Perkin Elmer). For metal-dependent processing assays, these metal solutions were diluted in buffer X (50 mM Tris, pH 7.0) to 1.3 mM. SodN was reduced with a 3-fold excess of DTT under anaerobic conditions and then buffer exchanged using Amicon Ultra – 0.5 mL centrifugal filters with 3-kDa MWCO pre-equilibrated with assay buffer M1 (50 mM Tris, pH 8.0). Metal-dependence of processing assays of SodN by SodX was carried out by mixing DTT-reduced SodN with purified SodX in absence or presence of metals in buffer solutions under anaerobic conditions. DTT-reduced SodN (40 μM) was incubated with 80 μM metals (Ni, Co, and Zn) in assay buffer M1 for 15 minutes. SodX (40 μM) was finally added to the reaction mixture and the samples were incubated at 30 ^{o}C for 12 hours. For protein composition analysis in the mixture by ESI-MS,100 μL of each of the metal-dependent processing assay samples was buffer exchanged in 5 mM ammonium acetate. These samples were then directly injected into AB Sciex QStar XL ESI-Q-TOF mass spectrometer, which was previously calibrated with PfHA. Analyst Software was then used to deconvolute the mass spectrum of each sample. The assay was also done in presence of 1mM TCEP in assay buffer M1 which yielded same results suggesting addition of TCEP does not change the cleavage outcome.

For L-Histidine or D-Histidine dependent processing assays in presence of nickel or cobalt, varying concentrations of L-His or D-His (0.01, 0.1, 1.0 and 10.0 mM) in assay buffer M2 (50 mM Tris, 1 mM TCEP, pH 8.0) were made. A stock solution of SodN was buffer exchanged in assay buffer M2 and diluted to 40 μM in each L-His containing buffer. A stock solution of $NiCl_2$ and $CoCl_2$ was also made in assay buffer M2. An aliquot of this nickel or cobalt solution was added to 40 μM SodN so that the final concentration of the metal is 80 μM and the assay mixture was incubated for 15 minutes. Then, an aliquot of SodX from its stock was then added to the assay mixture to produce a final concentration of 40 μM and incubated at 30 ^{o}C for 12 hours. As control, a sample with no metal was made similarly with 40 μM SodN and 40 μM SodX in assay buffer M2 containing 0.1 mM L-His. 100 μL of each of the L-His (or D-His) dependent processing assay samples were buffer exchanged in 5 mM ammonium acetate. These samples were then directly injected into pre-calibrated Thermo Orbitrap Fusion Tribrid. The data was deconvoluted using ThermoX Calibur Software from Thermo scientific.

Activity Assay

Kinetic measurements using pulse radiolytic production of superoxide.

For the negative (SodN) and positive (NiSOD) controls respectively, 150 μM of each of the protein in assay buffer M2 (50 mM Tris, 1 mM TCEP, pH 8.0) was mixed with 150 μM $NiCl_2$ (final concentration; made in assay buffer M2) and incubated for 16 h at 4 ^{o}C followed by addition of Chelex beads to remove excess nickel. For proteolytic mixtures, a 1:1 mixture of DTT-reduced SodN (150 μM) and SodX in assay buffer M2 (50 mM Tris, 1 mM TCEP, pH 8.0) or L-Histidine (0.01 mM, 0.1 mM, 1.0 mM) containing assay buffer M2 was incubated for 16 h at 30 ^{o}C. Similar to controls, 150 μM $NiCl_2$ (made in assay buffer M2) was then added to the

assay samples followed by addition of Chelex to remove excess nickel. All samples (holo-NiSOD, Ni-SodN, and the nickel containing proteolytic mixtures (SodN + SodX with or without L-histidine) were then buffer exchanged in buffer P containing 10 mM phosphate, 30 mM formate, pH 7.5 using Amicon Ultra – 0.5 mL centrifugal filters with 3-kDa MWCO (at least 10-12 rounds were done to ensure efficient buffer exchange). The nickel content of each of these samples was determined using ICP-MS (**Table S4**). The catalytic removal of superoxide radicals ($O_2^{\bullet-}$) by the various species described above was measured directly using pulse radiolysis at Brookhaven National Laboratory. The disappearance of $O_2^{\bullet-}$ was followed optically at 260 nm. The solutions were diluted ten times relative to Ni concentration and all contained micromolar concentrations of nickel in NiSOD, SodN, or mixtures thereof. All rate constants are given relative to the concentration of Ni determined by ICP in the buffer-exchanged sample. EDTA was added a few minutes prior to generation of $O_2^{\bullet-}$ and sequential pulses generating different amounts of $O_2^{\bullet-}$ were administered for 5-10 minutes. Although the catalytic activity of the cleavage product mixture is small (specific activity with respect to [Ni]= 3.7×10^7 $M^{-1}s^{-1}$) relative to the activity of purified NiSOD (0.7×10^9 $M^{-1}s^{-1}$)[18], it is much greater than observed for the spontaneous bimolecular disproportionation of $O_2^{\bullet-}$ at μM concentrations (~10^5 s^{-1}) or reaction mixtures that did not contain SodX. (**Fig. 6**). There was no significant change in rate from the initial to the final pulse. This procedure was used to ensure that EDTA was not removing Ni from an active site in SodN or SodX during the time of the experiment.

X-ray Absorption Spectroscopy (XAS)

1. Sample Preparation

NiSodN: A stock solution of 300 μM SodN protein was reduced with 3-fold excess of DTT under anaerobic conditions for three hours and then buffer exchanged in Buffer D (50 mM Tris, 200 mM NaBr, pH 8.0) using an Amicon Ultra – 0.5 mL centrifugal filters with 3-kDa MWCO pre-equilibrated with Buffer D. Aliquots of a $NiCl_2$ solution from stock (9.34 mM) were added to the SodN sample at an interval of 15 minutes until a 3-fold excess of nickel was reached, and then incubated for an additional 1 hour. Excess nickel from this sample was removed using Chelex beads (Sigma) and the sample was then concentrated to 100 μl. An aliquot from this sample was used to determine the nickel content using ICP-OES and protein concentration using UV-vis. The ratio of nickel bound per SodN protein was found to be 0.8. The remaining sample of Ni-SodN was mixed glycerol to 11% by volume and loaded into kapton-taped polycarbonate holders and then rapidly frozen in liquid nitrogen.

NiSodN•His: A stock solution of purified WT-SodN (0.72 mM in Buffer C (50 mM HEPES, 1 mM TCEP, pH 7.0) containing ~ 200 mM NaCl,1 mM EDTA and 10% glycerol) was buffer exchanged in Buffer X (50 mM Tris, 200 mM NaBr, 0.1 mM L-Histidine, pH 8.0) using Amicon Ultra – 0.5 mL centrifugal filters with 3-kDa MWCO that was pre-equilibrated with Buffer X. An aliquot of aqueous $NiCl_2$ solution (stock concentration 9.34 mM) was added to the diluted sample of WT-SodN (150 μM) in Buffer X in five-minute intervals on ice so that the final concentration of nickel in the sample is ~93.4 μM, and the sample mixture was incubated for 16 hours at 4 ^{o}C. To remove any unbound nickel, Chelex beads (Sigma) were added to the

sample and incubated for ten minutes at room temperature. The solution was then concentrated to ~70 µL using Amicon Ultra – 0.5 mL centrifugal filters with 3-kDa MWCO. An aliquot of this sample was used to determine the nickel content using ICP-MS and protein monomer concentration using UV-vis (ε = 17, 085 $M^{-1}cm^{-1}$). The final concentration of WT-SodN and nickel in the concentrated sample was found to be 0.9 mM and 0.134 mM, respectively. To the remaining sample of NiSodN•His, glycerol was added up to a final concentration of 10%, and the sample was loaded into the kapton-taped polycarbonate holders and then rapidly frozen in liquid nitrogen.

2. Data collection and reduction

XAS data on frozen samples of NiSodN and NiSodN•His immobilized on aluminum prongs and cooled to ~10K using a liquid helium cryostat (Oxford Instruments) were collected at the Stanford Synchrotron Radiation Lightsource (SSRL) using dedicated ring conditions (3 GeV and 450-500 mA) and Si(220) monochromators. The data on NiSodN were collected on beamline 9-3 using a Rh mirror left flat for harmonic rejection, while data for NiSodN•His was collected in remote operation mode on beamline 7-3, where harmonic rejection was achieved by detuning the monochromator by 50%. X-ray fluorescence data were collected using a 30-element Ge detector (Canberra). To minimize scattering, a 3 µm Z-1 filter and Soller slits were installed between the detector and sample. X-ray fluorescence data on the Ni K-edge of NiSodN and NiSodN•His were collected concurrently with spectra of Ni metal foil in transmission mode for energy calibration. Extended X-ray Absorption Fine Structure (EXAFS) were collected to 15k above the K-edge.

Data reduction and analyses were performed according to previously published procedures for Ni K-edge XAS data.[30, 51, 54, 63] The output of each channel of the 30-elelment Ge detector was evaluated. For NiSodN the spectra obtained from individual scans were summations from 23 elements. For NiSodN•His, the spectra utilized 29 channels. Each scan was calibrated to the first inflection point of the Ni-foil spectrum. Examination of the XANES data from individual scans for NiSodN showed that the sample was stable in the x-ray beam, and the analyzed spectrum (shown in **Fig. 3b-d**) was the sum of 8 scans. A similar examination of the XANES data from NiSodN•His revealed that the sample was unstable in the beam and exhibited an edge energy shift and changes in XANES features for the first 5 scans (**Fig. S10a**). For this reason, the data from the first and last scans (of eight) were analyzed separately. Analysis of individual scans was more limited by signal:noise in the case of NiSodN•His.

The Sixpack software package was used to process and normalize the XAS data.[64] For normalization and background correction, the K-edge energy of Ni was set to 8340 eV with an R_{bkg} of 1. A Gaussian function was used for fitting the pre-edge range of -200 to -50eV and quadratic polynomial functions with 7-8 spline points were used to fit the post-edge range of +100 to +975 eV relative to E_0. The edge jump was normalized by setting the difference between the corrected pre-edge and post-edge baselines to 1. The EXAFS data were converted to k-space using the relationship $[2m_e (E-E_0)/\hbar^2]^{1/2}$, where m_e is the mass of an electron and $\hbar$ is the Plank's constant divided by 2π. The k^3-weighted EXAFS data were Fourier-transformed over the k-range 2-12.5 $Å^{-1}$ using a Hanning window and fit in r-space using an S_0 value of 0.9. The r-space data shown in the figures was not corrected for phase shifts.

3. Data analysis

XANES analysis of the background-corrected and normalized spectra were performed using in Origin 9.1 by fitting Exponential Growth Function1 to fit the rising edge in the pre-edge region and integrate the peak areas to account for pre-edge XANES features. The fitting was performed in triplicate to obtain the errors. These features are associated with electronic transitions that involve the promotion of the core 1s electron to either the 3d manifold (1s → 3d), which occurs near 8331 eV, or to a $4p_z$ orbital (1s → $4p_z$), which occurs near 8336 eV. The intensities of these features provide information about the coordination number and geometry of the Ni site.[47]

The Artemis software program[64] was used for EXAFS analysis with parameters for scattering atoms generated by FEFF6. Multiple-scattering paths for histidine imidazole and backbone amide (BBAm) ligands were generated as previously described.[61] The EXAFS fitting equation used was:

$$\chi(k) = \sum_i \frac{N_i f_i(k) e^{-2k^2\sigma_i^2}}{kr_i^2} sin[\,2kr_i + \delta_i(k)] \quad (1)$$

where *f(k)* is the scattering amplitude, *δ(k)* is the phase-shift, *N* is the number of neighboring atoms, *r* is the distance to the neighboring atoms, and σ_i^2 is a Debye-Waller factor reflecting the mean square deviation in the distance to the nearest neighbor (thermal and static disorder).

To compare the different models fit to the data set, ifeffit utilizes three goodness of fit parameters: χ^2, reduced χ^2 , and the R-factor. χ^2 is given by equation 2, where N_{idp} is the number

of independent data points, N_ε^2 is the number of uncertainties to minimize, Re(fi) is the real part of EXAFS function and Im(fi) is the imaginary part of the EXAFS fitting function.

$$\chi^2 = \frac{N_{idp}}{N_{\varepsilon 2}}\{[Re(fi)2] + [Im(fi)2]\} \qquad (2)$$

Reduced χ^2 represents the degree of freedom in the fit and is given by equation (3),

$$red.\chi^2 = \frac{\chi^2}{N_{\text{idp}} - N_{\text{var}}} \qquad (3)$$

where N_{var} is the number of refining parameters and N_{var} is the number of adjustable parameters. Additionally, ifeffit calculates the R-factor for the fit, which is given by equation (4) and is scaled to the magnitude of the data making it proportional to χ^2.

$$\text{R} = \frac{\sum_{i=1}^{N}\{[Re(f_i)^2]+[Im(f_i)^2]\}}{\sum_{i=1}^{N}\{[Re(xdata_i)]^2+[Im(xdata_i)]^2\}} \qquad (4)$$

In comparing different models, the R-factor and reduced χ^2 parameter were used to determine the model that was the best fit for the data. A good fit corresponds to an R-factor <5%. The R-factor will generally improve with an increasing number of adjustable parameters, while reduced χ^2 will go through a minimum and then increase, indicating that the model is overfitting the data. The resolution of the data was determined by equation (5).

$$\text{Resolution} = \frac{\pi}{2\Delta k} \qquad (5)$$

Tables S6 -8 summarize the development of models used to generate the best fits to the Fourier-transformed EXAFS data over the r-range of 1.0 - 4.0 Å of NiSodN, and the first and last scan of NiSodN•His, respectively (**Fig. S10**, **Table S5-7**).

For NiSodN, single-scattering analysis of EXAFS data employing a single shell of scattering atoms is consistent with a five- or six-coordinate Ni(II) site composed of N/O-donor ligands (**Table S5**). A six-coordinate nickel site is consistent with the coordination number/geometry determined from the XANES analysis. Including one or two S-donor shells in the fits improves the R-factor but gives unacceptable values of σ^2 (disorder) for the S shells. Splitting the single shell of six N/O-donors into two shells of N/O-donors with 5 N/O-donors at 2.08 Å and 1 N/O-donor at 2.28 Å improved the values of σ^2 and also lowered the R-factor. Substituting the long N/O ligand with 1 imidazole ligand further improves the R-factor by accounting for scattering in the second and third coordination sphere of the Ni center, but increases the values of σ^2 for the remaining shell of 5 N/O-donors. Modeling two of the N/O ligands as a bidentate amidate ligand (BBAm), a known feature of Ni coordination in NiSOD, as has been done for other complexes where backbone N coordination leads to the formation of a five-membered chelate ring[61], further improved the fit and gave acceptable values for σ^2. Finally, adjusting the single imidazole ligand to a tilt angle of $\alpha = 5^o$ in the model with bidentate amidate coordination further lowers the R-factor to 4.1% with acceptable value of σ^2 for each shell, and hence was the best fit model (**Fig. 3c-d**). Attempts to Include S-donors in this model again resulted in better R-factors but had unacceptable values of σ^2 for these donors. Incorporation of two imidazole ligands in the model further improved the R-factor, but results in higher a σ^2 value for the long N/O ligand. The best fit model is consistent with the absence of S-donors (*e.g.,*thiolates from cysteines, Cys 16 or 20 in the *Sc* SodN amino acid sequence) and with one of the six N/O-donor ligands contributed by an imidazole from histidine, most likely the His15 in SodN.

Because of the photosensitivity in the beam (Fig. **S10a**), the EXAFS for NiSodN•His corresponding to the first and last of these scans were analyzed separately (**Table S6, S7**). Single-scattering analysis of the EXAFS data of the final scan of NiSodN•His complex (**Fig. 3e-f**) indicates that the nickel site in this complex is better fit by a model containing four- or five- S-donors than a corresponding single N/O-donor shell (**Table S6**). A four- or five- coordinate mixed shell consisting of 1-2 S- donors at 2.18-2.22 Å with 2-4 N/O- donors at 1.96-2.06 Å improved the fits by lowering the R-factor and reducing χ^2. Splitting the N/O- shell improved the fitting parameters but also introduced unacceptable values of σ^2 for either the long N- or S-donors or both in some fits. Substituting the longer N/O-donor with one imidazole ligand in these fits resulted in four or five-coordinate fits, $[Ni(N/O)_{2\text{-}3}(Im)S]$ with acceptable σ^2 values for each shell of N- and S-donors and an R-factor below 5% and are among the best fits (**Fig. 3e,f**). Addition of a shell containing a S-donor at 2.58 Å (**Fig. S10b**) improves the fit slightly, but has large values of σ^2 (disorder). Since a weakly bound ligand might be very disordered, it cannot be ruled out and remains a possibility. Cys16 and/or Cys20 are the likely candidates for S-coordination, while the imidazole ligand could be His15 or provided by the L-Histidine in the medium. These models are also consistent with the XANES analysis showing a 4- or 5-coordinate Ni site. A similar analysis of the first scan of the data from NiSodN•His, gave similar best fit models (**Table S7**).

References

1. Ackerman CM, Lee S, Chang CJ. Analytical Methods for Imaging Metals in Biology: From Transition Metal Metabolism to Transition Metal Signaling. *Anal. Chem.* 2017;**89**(1):22-41. doi: 10.1021/acs.analchem.6b04631
2. Chandrangsu P, Rensing C, Helmann JD. Metal homeostasis and resistance in bacteria. *Nat. Rev. Microbiol.* 2017;**15**(6):338-50. doi: 10.1038/nrmicro.2017.15
3. Brawley HN, Lindahl PA. Low-molecular-mass labile metal pools in Escherichia coli: advances using chromatography and mass spectrometry. *J. Biol. Inorg. Chem.* 2021. doi: 10.1007/s00775-021-01864-w
4. Callahan DL, Baker AJ, Kolev SD, Wedd AG. Metal ion ligands in hyperaccumulating plants. *J. Biol. Inorg. Chem.* 2006;**11**(1):2-12. doi: 10.1007/s00775-005-0056-7
5. Montargès-Pelletier E, Chardot V, Echevarria G, Michot LJ, Bauer A, Morel J-L. Identification of nickel chelators in three hyperaccumulating plants: An X-ray spectroscopic study. *Phytochemistry* 2008;**69**(8):1695-709. doi: https://doi.org/10.1016/j.phytochem.2008.02.009
6. Callahan DL, Roessner U, Dumontet V, Perrier N, Wedd AG, O'Hair RA, Baker AJ, Kolev SD. LC-MS and GC-MS metabolite profiling of nickel(II) complexes in the latex of the nickel-hyperaccumulating tree Sebertia acuminata and identification of methylated aldaric acid as a new nickel(II) ligand. *Phytochemistry* 2008;**69**(1):240-51. doi: 10.1016/j.phytochem.2007.07.001
7. Foster AW, Pernil R, Patterson CJ, Scott AJP, Palsson LO, Pal R, Cummins I, Chivers PT, Pohl E, Robinson NJ. A tight tunable range for Ni(II) sensing and buffering in cells. *Nat. Chem. Biol.* 2017;**13**(4):409-14. doi: 10.1038/nchembio.2310
8. Chivers PT, Benanti EL, Heil-Chapdelaine V, Iwig JS, Rowe JL. Identification of Ni-(L-His)(2) as a substrate for NikABCDE-dependent nickel uptake in Escherichia coli. *Metallomics* 2012;**4**(10):1043-50. doi: 10.1039/c2mt20139a
9. Chivers PT. Nickel recognition by bacterial importer proteins. *Metallomics* 2015;**7**(4):590-5. doi: 10.1039/c4mt00310a
10. Youn HD, Kim EJ, Roe JH, Hah YC, Kang SO. A novel nickel-containing superoxide dismutase from Streptomyces spp. *The Biochemical journal* 1996;**318 (Pt 3)**:889-96
11. Lee JW, Roe JH, Kang SO. Nickel-containing superoxide dismutase. *Methods in enzymology* 2002;**349**:90-101
12. Barondeau DP, Kassmann CJ, Bruns CK, Tainer JA, Getzoff ED. Nickel superoxide dismutase structure and mechanism. *Biochemistry* 2004;**43**(25):8038-47. doi: 10.1021/bi0496081
13. Bryngelson PA, Arobo SE, Pinkham JL, Cabelli DE, Maroney MJ. Expression, reconstitution, and mutation of recombinant Streptomycescoelicolor NiSOD. *J. Am. Chem. Soc.* 2004;**126**(2):460-1. doi: 10.1021/ja0387507
14. Ahn BE, Cha J, Lee EJ, Han AR, Thompson CJ, Roe JH. Nur, a nickel-responsive regulator of the Fur family, regulates superoxide dismutases and nickel transport in Streptomyces coelicolor. *Molecular microbiology* 2006;**59**(6):1848-58. doi: 10.1111/j.1365-2958.2006.05065.x
15. Miller A-F. Superoxide dismutases: ancient enzymes and new insights. *FEBS Lett.* 2012;**586**(5):585-95. doi: 10.1016/j.febslet.2011.10.048
16. Cuvelier ML, Allen AE, Monier A, McCrow JP, Messié M, Tringe SG, Woyke T, Welsh RM, Ishoey T, Lee J-H, Binder BJ, DuPont CL, Latasa M, Guigand C, Buck KR, Hilton J, Thiagarajan M, Caler E, Read B, Lasken RS, Chavez FP, Worden AZ. Targeted metagenomics

and ecology of globally important uncultured eukaryotic phytoplankton. *Proc. Natl. Acad. Sci. U.S.A.* 2010;**107**(33):14679-84. doi: 10.1073/pnas.1001665107
17. Wuerges J, Lee JW, Yim YI, Yim HS, Kang SO, Djinovic Carugo K. Crystal structure of nickel-containing superoxide dismutase reveals another type of active site. *Proc. Natl. Acad. Sci. U S A* 2004;**101**(23):8569-74. doi: 10.1073/pnas.0308514101
18. Choudhury SB, Lee JW, Davidson G, Yim YI, Bose K, Sharma ML, Kang SO, Cabelli DE, Maroney MJ. Examination of the nickel site structure and reaction mechanism in Streptomyces seoulensis superoxide dismutase. *Biochemistry* 1999;**38**(12):3744-52. doi: 10.1021/bi982537j
19. Sheng Y, Abreu IA, Cabelli DE, Maroney MJ, Miller AF, Teixeira M, Valentine JS. Superoxide dismutases and superoxide reductases. *Chem. Rev.* 2014;**114**(7):3854-918. doi: 10.1021/cr4005296
20. Deborah Zamble MR-Z, Henryk Kozlowski. *The Biological Chemistry of Nickel.* Cambridge, U.K.: Royal Society of Chemistry, 2017
21. Campecino JO, Maroney, M.J. Reinventing the Wheel: The NiSOD Story. In: Deborah Zamble MR-Z, Henryk Kozlowskis (ed). *The Biological Chemistry of Nickel*. Metallobiology Series No. 10: Royal Society of Chemistry, 2017
22. Kim EJ, Chung HJ, Suh B, Hah YC, Roe JH. Transcriptional and post-transcriptional regulation by nickel of sodN gene encoding nickel-containing superoxide dismutase from Streptomyces coelicolor Muller. *Mol. Microbiol.* 1998;**27**(1):187-95. doi: 10.1046/j.1365-2958.1998.00674.x
23. Bryngelson PA, Arobo SE, Pinkham JL, Cabelli DE, Maroney MJ. Expression, reconstitution, and mutation of recombinant Streptomycescoelicolor NiSOD. *J. Am. Chem. Soc.* 2004;**126**(2):460-1. doi: 10.1021/ja0387507
24. Kim IK, Yim YI, Kim YM, Lee JW, Yim HS, Kang SO. CbiX-homologous protein (CbiXhp), a metal-binding protein, from Streptomyces seoulensis is involved in expression of nickel-containing superoxide dismutase. *FEMS Microbiol. Lett.* 2003;**228**(1):21-6. doi: 10.1016/s0378-1097(03)00719-5
25. Eitinger T. In vivo production of active nickel superoxide dismutase from Prochlorococcus marinus MIT9313 is dependent on its cognate peptidase. *J. Bacteriol.* 2004;**186**(22):7821-5. doi: 10.1128/jb.186.22.7821-7825.2004
26. Senger M, Stripp ST, Soboh B. Proteolytic cleavage orchestrates cofactor insertion and protein assembly in [NiFe]-hydrogenase biosynthesis. *J. Biol. Chem.* 2017;**292**(28):11670-81. doi: 10.1074/jbc.M117.788125
27. Lacasse MJ, Zamble DB. [NiFe]-Hydrogenase Maturation. *Biochemistry* 2016;**55**(12):1689-701. doi: 10.1021/acs.biochem.5b01328
28. Wuerges J, Lee JW, Yim YI, Yim HS, Kang SO, Djinovic Carugo K. Crystal structure of nickel-containing superoxide dismutase reveals another type of active site. *Proc. Natl. Acad. Sci. U. S. A.* 2004;**101**(23):8569-74. doi: 10.1073/pnas.0308514101
29. Butre CI, Buhler S, Sforza S, Gruppen H, Wierenga PA. Spontaneous, non-enzymatic breakdown of peptides during enzymatic protein hydrolysis. *Biochim. Biophys. Acta* 2015;**1854**(8):987-94. doi: 10.1016/j.bbapap.2015.03.004
30. Huang HT, Dillon S, Ryan KC, Campecino JO, Watkins OE, Cabelli DE, Brunold TC, Maroney MJ. The Role of Mixed Amine/Amide Ligation in Nickel Superoxide Dismutase. *Inorg. Chem.* 2018;**57**(20):12521-35. doi: 10.1021/acs.inorgchem.8b01499

31. Basak P, Zambelli B, Cabelli DE, Ciurli S, Maroney MJ. Pro5 is not essential for the formation of 'Ni-hook' in nickel superoxide dismutase. *J. Inorg. Biochem.* 2022;**234**:111858. doi: https://doi.org/10.1016/j.jinorgbio.2022.111858
32. Fiedler AT, Bryngelson PA, Maroney MJ, Brunold TC. Spectroscopic and computational studies of Ni superoxide dismutase: electronic structure contributions to enzymatic function. *J. Am. Chem. Soc.* 2005;**127**(15):5449-62. doi: 10.1021/ja042521i
33. UniProt: a worldwide hub of protein knowledge. *Nucleic Acids Research* 2019;**47**:D506-15
34. Kilcoyne M, Gerlach JQ, Farrell MP, Bhavanandan VP, Joshi L. Periodic acid-Schiff's reagent assay for carbohydrates in a microtiter plate format. *Anal. Biochem.* 2011;**416**(1):18-26. doi: 10.1016/j.ab.2011.05.006
35. Riener CK, Kada G, Gruber HJ. Quick measurement of protein sulfhydryls with Ellman's reagent and with 4,4'-dithiodipyridine. *Anal. Bioanal. Chem.* 2002;**373**(4-5):266-76. doi: 10.1007/s00216-002-1347-2
36. Auld DS. [14] Removal and replacement of metal ions in metallopeptidases. *Methods in enzymology*: Academic Press, 1995, 228-42
37. Paetzel M, Dalbey RE, Strynadka NC. Crystal structure of a bacterial signal peptidase in complex with a beta-lactam inhibitor. *Nature* 1998;**396**(6707):186-90. doi: 10.1038/24196
38. Peters DS, Romesberg FE, Baran PS. Scalable Access to Arylomycins via C–H Functionalization Logic. *J. Am. Chem. Soc.* 2018;**140**(6):2072-5. doi: 10.1021/jacs.8b00087
39. M. P. Bacterial Signal Peptidases. *Subcell Biochem.* 2019;**92**:187-219
40. Paetzel M, Goodall JJ, Kania M, Dalbey RE, Page MG. Crystallographic and biophysical analysis of a bacterial signal peptidase in complex with a lipopeptide-based inhibitor. *J. Biol. Chem.* 2004;**279**(29):30781-90. doi: 10.1074/jbc.M401686200
41. Kelley LA, Mezulis S, Yates CM, Wass MN, Sternberg MJ. The Phyre2 web portal for protein modeling, prediction and analysis. *Nat. Protoc.* 2015;**10**(6):845-58. doi: 10.1038/nprot.2015.053
42. Herbst RW, Guce A, Bryngelson PA, Higgins KA, Ryan KC, Cabelli DE, Garman SC, Maroney MJ. Role of conserved tyrosine residues in NiSOD catalysis: a case of convergent evolution. *Biochemistry* 2009;**48**(15):3354-69. doi: 10.1021/bi802029t
43. Zhang Y, Akilesh S, Wilcox DE. Isothermal Titration Calorimetry Measurements of Ni(II) and Cu(II) Binding to His, GlyGlyHis, HisGlyHis, and Bovine Serum Albumin: A Critical Evaluation. *Inorg. Chem.* 2000;**39**(14):3057-64. doi: 10.1021/ic000036s
44. Bennett BD, Kimball EH, Gao M, Osterhout R, Van Dien SJ, Rabinowitz JD. Absolute metabolite concentrations and implied enzyme active site occupancy in Escherichia coli. *Nat. Chem. Bio.* 2009;**5**(8):593-9. doi: 10.1038/nchembio.186
45. Osman D, Martini MA, Foster AW, Chen J, Scott AJP, Morton RJ, Steed JW, Lurie-Luke E, Huggins TG, Lawrence AD, Deery E, Warren MJ, Chivers PT, Robinson NJ. Bacterial sensors define intracellular free energies for correct enzyme metalation. *Nat. Chem. Biol.* 2019;**15**(3):241-9. doi: 10.1038/s41589-018-0211-4
46. Blackburn JR, Jones MM. Stereoselectivity in the metal complex catalyzed hydrolysis of amino acid esters—II The role of a catalyst structure. *Journal of Inorganic and Nuclear Chemistry* 1973;**35**(5):1597-603. doi: https://doi.org/10.1016/0022-1902(73)80251-9
47. Colpas GJ, Maroney MJ, Bagyinka C, Kumar M, Willis WS, Suib SL, Mascharak PK, Baidya N. X-ray spectroscopic studies of nickel complexes, with application to the structure of nickel sites in hydrogenases. *Inorg. Chem.* 1991;**30**(5):920-8. doi: 10.1021/ic00005a010

48. Xia J, Dong J, Wang S, Scott RA, Lindahl PA. EXAFS, EPR, and Electronic Absorption Spectroscopic Study of the .alpha. Metallo Subunit of CO Dehydrogenase from Clostridium thermoaceticum. *J. Am. Chem. Soc.* 1995;**117**(27):7065-70. doi: 10.1021/ja00132a004
49. Tan GO, Ensign SA, Ciurli S, Scott MJ, Hedman B, Holm RH, Ludden PW, Korszun ZR, Stephens PJ, Hodgson KO. On the structure of the nickel/iron/sulfur center of the carbon monoxide dehydrogenase from Rhodospirillum rubrum: an x-ray absorption spectroscopy study. *Proc. Nat. Acad. Sci. USA* 1992;**89**(10):4427. doi: 10.1073/pnas.89.10.4427
50. Colpas GJ, Kumar M, Day RO, Maroney MJ. Structural investigations of nickel complexes with nitrogen and sulfur donor ligands. *Inorg. Chem.* 1990;**29**(23):4779-88. doi: 10.1021/ic00348a037
51. Ryan KC, Guce AI, Johnson OE, Brunold TC, Cabelli DE, Garman SC, Maroney MJ. Nickel superoxide dismutase: structural and functional roles of His1 and its H-bonding network. *Biochemistry* 2015;**54**(4):1016-27. doi: 10.1021/bi501258u
52. Iwig JS, Leitch S, Herbst RW, Maroney MJ, Chivers PT. Ni(II) and Co(II) sensing by Escherichia coli RcnR. *J. Am. Chem. Soc.* 2008;**130**(24):7592-606. doi: 10.1021/ja710067d
53. Lebrette H, Brochier-Armanet C, Zambelli B, de Reuse H, Borezée-Durant E, Ciurli S, Cavazza C. Promiscuous nickel import in human pathogens: structure, thermodynamics, and evolution of extracytoplasmic nickel-binding proteins. *Structure* 2014;**22**(10):1421-32. doi: 10.1016/j.str.2014.07.012
54. Ryan KC, Johnson OE, Cabelli DE, Brunold TC, Maroney MJ. Nickel superoxide dismutase: structural and functional roles of Cys2 and Cys6. *J. Biol. Inorg. Chem.* 2010;**15**(5):795-807. doi: 10.1007/s00775-010-0645-y
55. Milan Melnik, Tibor Sramko, Michal Dunaj--Jurco, Anton Sirota, Clive E. Hollow Ay. Nickel coordination compounds: Classification and analysis of crystallographic and structural data. *Rev. Inorg.Chem.* 1994;**14**(1-4):1. doi: https://doi.org/10.1515/REVIC.1994.14.1-4.1
56. Rosenfield SG, Berends HP, Gelmini L, Stephan DW, Mascharak PK. New octahedral thiolato complexes of divalent nickel: syntheses, structures, and properties of (Et4N)[Ni(SC5H4N)3] and (Ph4P)[Ni(SC4H3N2)3].CH3CN. *Inorg. Chem.* 1987;**26**(17):2792-7. doi: 10.1021/ic00264a015
57. Theodoratou E, Paschos A, Magalon A, Fritsche E, Huber R, Bock A. Nickel serves as a substrate recognition motif for the endopeptidase involved in hydrogenase maturation. *Eur. J. Biochem.* 2000;**267**(7):1995-9. doi: 10.1046/j.1432-1327.2000.01202.x
58. Menon AL, Robson RL. In vivo and in vitro nickel-dependent processing of the [NiFe] hydrogenase in Azotobacter vinelandii. *J. Bacteriol.* 1994;**176**(2):291-5. doi: 10.1128/jb.176.2.291-295.1994
59. Magalon A, Blokesch M, Zehelein E, Bock A. Fidelity of metal insertion into hydrogenases. *FEBS Lett.* 2001;**499**(1-2):73-6. doi: 10.1016/s0014-5793(01)02525-x
60. Blokesch M, Böck A. Maturation of [NiFe]-hydrogenases in Escherichia coli: the HypC cycle. *J. Mol. Biol.* 2002;**324**(2):287-96. doi: 10.1016/s0022-2836(02)01070-7
61. Hu HQ, Johnson RC, Merrell DS, Maroney MJ. Nickel Ligation of the N-Terminal Amine of HypA Is Required for Urease Maturation in Helicobacter pylori. *Biochemistry* 2017;**56**(8):1105-16. doi: 10.1021/acs.biochem.6b00912
62. Dahlqvist A, Olsson I, Nordén Å. The periodate-schiff reaction: Specificity, kinetics, and reaction products with pure substrates. *J. Histochem. & Cytochem.* 1965;**13**(6):423-30. doi: 10.1177/13.6.423

63. Campecino JO, Dudycz LW, Tumelty D, Berg V, Cabelli DE, Maroney MJ. A Semisynthetic Strategy Leads to Alteration of the Backbone Amidate Ligand in the NiSOD Active Site. *J. Am. Chem. Soc.* 2015;**137**(28):9044-52. doi: 10.1021/jacs.5b03629
64. Webb SM. SIXPack a Graphical User Interface for XAS Analysis Using IFEFFIT. *Physica Scripta* 2005:1011. doi: 10.1238/physica.topical.115a01011

Acknowledgments

The authors acknowledge support for this work from the NIH R01-GM069696 (MJM). We thank Kelsey Clements for cloning *sodX* from *S. coelicolor* genomic DNA into pET15bSUMO vector. XAS data collection was performed at the Stanford Synchrotron Radiation Light (SSRL) source, a national user facility operated by Stanford University on behalf of U.S. Department of Energy, Office of Basic Energy Sciences. The SSRL Structural and Molecular Biology Program is supported by the Department of Energy, Office of Biological Environmental Research, and by the National Institutes of Health, National Center for Research Resources, Biomedical Technology Program. Mass-Spectrometry experiments were performed at the mass spectrometry facility at Institute for Applied Life Sciences (IALS), University of Massachusetts Amherst. SEC-MALS and CD experiments were performed at the Biophysical Characterization Core Facility, part of the IALS at the University of Massachusetts Amherst. We also thank David S. Peters and Floyd E. Romesberg, Phil S. Baran, at Department of Chemistry, The Scripps Research Institute for providing the inhibitor for the protease.

Author Contributions

P. B prepared the samples and performed the biochemical, biophysical and spectroscopic experiments, their analysis, interpretation, and manuscript drafting. D.E.C performed pulse radiolysis experiments, analyzed the data, and drafted the manuscript, E.R.F collected part of the XAS data. M.J.M and P.T.C designed the project, interpreted the data, and wrote the manuscript.

Competing Financial Interests

The authors declare no competing financial interests.

Data Availability Statement: Data available upon request to the authors.

For Table of Contents only

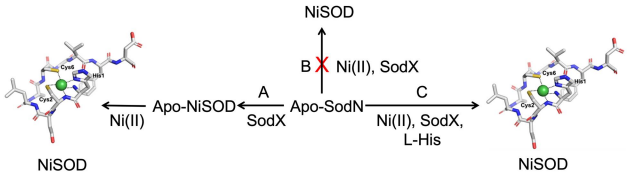

Table 1. SodN characterization parameters determined using mass spectrometry, ITC and UV-visible spectroscopy.

[a] Monomer masses determined using mass spectrometry under denaturing conditions.
[b] Nickel binding parameters obtained using Isothermal Titration Calorimetry.

Protein	**Theoretical Monomer Mass (Da)**	**[a]Observed Monomer Mass (Da)**	**[b]Ni-binding parameters**		**[c]LMCT S→Ni(III)**	**[a]Processing**
			K_d (μM)	n		
Apo-NiSOD	13,200.1	13,199.1	0.025(20)[f] 0.250(60)[f]	0.38(3)[f] 0.68(6)[f]	Yes	NA[d]
SodN	14,702.8	14,701.8	21.1(2)	1.03(2)	No	Yes[e]
H15A-SodN	14,636.8	14,635.3	20.8(2)	0.47(2)	No	No

[c] Spectral features obtained from UV-Visible spectroscopy.
[d] NA = Not applicable
[e] Cleavage product with correct mass (13,199 Da) detected by mass spectrometry.
[f] Binding parameters of apo-NiSOD were adapted from Ref.2 and represent the values assigned to *cis*- and *trans*-conformations of Pro5.

Table 2: Comparison of the best fit models of Ni K-edge EXAFS for NiSodN and NiSodN•His.

Shell	R (Å)	σ^2 (x10^{-3} Å^{-2})	ΔE_0	R-factor(%)
		NiSodN		
2 N/O	**2.08(2)**	**1(2)**		
1 N/O	**2.25(4)**	**1(3)**		
1 Im(5°)	**2.13(2)**	**1(2)**		
1BBAm (2 N)	**1.99(3), 2.04(3)**	**4(3)**	**3(1)**	**4.1**
		NiSodN•His (Last scan)		
2 N/O	**2.03(2)**	**3(1)**		
1 Im	**1.98(4)**	**6(4)**		
1 S	**2.22(1)**	**4(1)**	**0(2)**	**3.9**
3 N/O	2.06(2)	7(3)		
1 Im	2.01(3)	6(3)		
1 S	2.21(3)	5(2)	2(1)	3.3
2 N/O	2.03(2)	3(1)		
1 Im	2.02(4)	6(4)		
1 S	2.25(1)	4(1)		
1 S	2.58(1)	14(1)	0(2)	2.3
		NiSodN•His (First scan)		
2 N/O	2.01(2)	4(2)		
1 Im	2.00(3)	4(3)		
1 S	2.23(1)	2(1)	1(1)	3.6
3 N/O	2.03(2)	9(2)		
1 Im	2.02(2)	3(2)		
1 S	2.22(1)	3(1)	2(1)	2.9
2 N/O	2.01(1)	4(1)		
1 Im	2.02(2)	3(4)		
1 S	2.24(1)	2(2)		
1 S	2.55(3)	15(6)	3(1)	2.3

*BBAm implies Backbone amidate ligand that include coordination of two N atoms in the fit (see Methods for details)